

THE VERTICAL-CURRENT APPROXIMATION NONLINEAR FORCE-FREE FIELD CODE—DESCRIPTION, PERFORMANCE TESTS, AND MEASUREMENTS OF MAGNETIC ENERGIES DISSIPATED IN SOLAR FLARES

Markus J. Aschwanden

Lockheed Martin, Solar and Astrophysics Laboratory, Org. A021S, Bldg. 252, 3251 Hanover Street, Palo Alto, CA 94304, USA; aschwanden@lmsal.com
Received 2016 February 1; accepted 2016 April 11; published 2016 June 8

ABSTRACT

In this work we provide an updated description of the Vertical-Current Approximation Nonlinear Force-Free Field (VCA-NLFFF) code, which is designed to measure the evolution of the potential, non-potential, free energies, and the dissipated magnetic energies during solar flares. This code provides a complementary and alternative method to existing traditional NLFFF codes. The chief advantages of the VCA-NLFFF code over traditional NLFFF codes are the circumvention of the unrealistic assumption of a force-free photosphere in the magnetic field extrapolation method, the capability to minimize the misalignment angles between observed coronal loops (or chromospheric fibril structures) and theoretical model field lines, as well as computational speed. In performance tests of the VCA-NLFFF code, by comparing with the NLFFF code of Wiegelmann, we find agreement in the potential, non-potential, and free energy within a factor of \lesssim 1.3, but the Wiegelmann code yields in the average a factor of 2 lower flare energies. The VCA-NLFFF code is found to detect decreases in flare energies in most X, M, and C-class flares. The successful detection of energy decreases during a variety of flares with the VCA-NLFFF code indicates that current-driven twisting and untwisting of the magnetic field is an adequate model to quantify the storage of magnetic energies in active regions and their dissipation during flares. The VCA-NLFFF code is also publicly available in the Solar SoftWare.

Key words: Sun: flares - Sun: magnetic fields - Sun: UV radiation

1. INTRODUCTION

The measurement of the magnetic field in the solar corona is one of the major challenges in solar physics, while measurements of the photospheric field is a long-standing industry. Some researchers state that the coronal field cannot be measured (directly), but we take the standpoint here that a successful modeling method that matches the observed coronal loop geometries actually equates to a real measurement of the coronal magnetic field. The knowledge of the coronal magnetic field is paramount in many problems in solar physics, such as coronal seismology, coronal heating, magnetic energy storage, solar wind, magnetic instabilities, magnetic reconnection, and magnetic energy dissipation in solar flares and coronal mass ejections (CMEs), which further ties into the global energetics of particle acceleration and propagation in the coronal and heliospheric plasma. While a potential-field model is a suitable tool to explain the approximate geometry of coronal loops, a more important capability is the non-potential or free energy, which can be liberated in the solar corona and is able to trigger magnetic instabilities and to drive eruptive phenomena on the Sun and stars.

Traditional methods compute the magnetic field in the solar corona by potential-field extrapolation of the photospheric line-of-sight component $B_z(x, y)$ of the magnetic field, or by force-free extrapolation of the photospheric three-dimensional (3D) vector field B(x, y). Although these methods have been widely and frequently used in the solar physics community during the last three decades, inconsistencies with the observed geometry of coronal loops have been noticed recently (DeRosa et al. 2009; Sandman et al. 2009), since coronal loops are supposed to accurately trace out the magnetic field in a low plasma- β corona (Gary 2001). Misalignment angles between theoretical nonlinear force-free field (NLFFF) solutions and observed loop

directions amount to $\mu \approx 24^\circ - 44^\circ$ for both potential and non-potential-field models (DeRosa et al. 2009). Several studies have been carried out to pin down the uncertainties of NLFFF codes, investigating insufficient fields of view (FOVs), the influence of the spatial resolution, insufficient constraints at the computation box boundaries, and the violation of the force-free assumption in the lower chromosphere (Metcalf et al. 2008; DeRosa et al. 2009, 2015), but a solution to reconcile theoretical magnetic field models with the observed geometry of coronal loops has not been achieved yet and requires a new approach.

Thus there are two different types of NLFFF codes. The first type is the traditional NLFFF code that uses the 3D vector field $\boldsymbol{B}(x, y) = [B_x(x, y), B_y(x, y), B_z(x, y)]$ from a vector magnetograph as input for the photospheric boundary and uses an extrapolation scheme to compute magnetic field lines in coronal heights that are consistent with the photospheric boundary condition and fulfill the divergence-freeness and the force-freeness conditions. Examples and comparisons of such recent NLFFF codes are given in Metcalf et al. (2008) and DeRosa et al. (2009, 2015), which include the optimization method (Wheatland et al. 2000; Wiegelmann 2004; Wiegelmann et al. 2006, 2008; Wiegelmann & Inhester 2010), the magneto-frictional method (Valori et al. 2007, 2010), the Grad-Rubin method (Amari et al. 2006; Wheatland 2007), the conservation-element/solution-element spacetime (CESE-MHD-NLFFF: Jiang & Feng 2013), and other methods.

The second type is an alternative NLFFF code, which uses only the line-of-sight magnetogram $B_z(x, y)$ to constrain the potential field, while forward-fitting of an analytical approximation of a special NLFFF solution in terms of vertical currents to (automatically traced) coronal (or chromospheric) loop coordinates [x(s), y(s)] is carried out in order to determine the nonlinear force-free α -parameters for a number of unipolar (subphotospheric) magnetic sources. The theory of

the vertical-current approximation is originally derived in Aschwanden (2013a), while the numeric code (called the Vertical-Current Approximation Nonlinear Force-Free Field (VCA-NLFFF) code here) has been continuously developed and improved in a number of previous studies (Aschwanden & Sandman 2010; Sandman & Aschwanden 2011; Aschwanden et al. 2012, 2014a, 2014b, Aschwanden 2013a, 2013b, 2013c, 2015; Aschwanden & Malanushenko 2013). Because the recent developments have now reached an unprecedented level of accuracy in the determination of non-potential magnetic energies, it is timely to provide a comprehensive description and performance tests of the latest version of the VCA-NLFFF method. A related forward-fitting code, using a quasi-Grad-Rubin method to match a NLFFF solution to observed coronal loops has been pioneered independently (Malanushenko et al. 2009, 2011, 2012, 2014).

In this study we provide a short analytical description of the VCA-NLFFF method. We start with a description of the organization of the code (Section 2), and proceed with the three major parts of the code: (i) the determination of the potential field (Section 3), (ii) the automated tracing of coronal and chromospheric curvi-linear structures (Section 4), and the forward-fitting of the VCA-NLFFF model to the observed loop geometries (Section 5). Besides brief analytical descriptions, we provide extensive performance tests using recently published Atmospheric Imager Assembly (AIA; Lemen et al. 2012) and Helioseismic Magnetic Imager (HMI; Scherrer et al. 2012) data from the Solar Dynamics Observatory (SDO; Pesnell et al. 2011), with particular emphasis on the determination of the time evolution of the free (magnetic) energy in active regions and the dissipation of magnetic energies during X-class flares. Discussions and conclusions are provided in Sections 6 and 7.

2. ORGANIZATION OF THE VCA-NLFFF CODE

In contrast to traditional NLFFF codes, such as the optimization method (Wheatland et al. 2000; Wiegelmann & Inhester 2010), the magneto-frictional method (Valori et al. 2007, 2010), or the Grad-Rubin method (Wheatland 2007; Amari et al. 2006), which all are designed to match photospheric data, the VCA-NLFFF code developed here is designed to match coronal as well as chromospheric data, a capability that does not exist in traditional NLFFF codes. The VCA-NLFFF code has a modular architecture, which can be grouped into three major sections: (1) the decomposition of a magnetic line-of-sight map into a number of magnetic charges; (2) the automated feature recognition of curvi-linear features in coronal (extreme-UV (EUV)) and chromospheric (UV) images; and (3) the forward-fitting of a non-potential magnetic field model to the observed curvi-linear patterns of coronal loops or chromospheric fibrils, which we will describe in turn. A flow chart of the various modules of the VCA-NLFFF code is depicted in Figure 1.

2.1. Time Grid

The initial input for a series of runs is specified by a starting time $t_{\rm start}$ (in the format of universal time, UT), a desired time interval for the entire duration $(t_{\rm dur})$ of magnetic field computations, a time cadence $(t_{\rm cad})$, a heliographic position in longitude $l(t=t_{\rm start})$ and latitude $b(t=t_{\rm start})$ for the center of the chosen FOV specified at the starting time, and a desired

FOV size for a rectangular subimage (in Cartesian coordinates) in which a solution of the magnetic field is computed. The subimage should be chosen inside the solar disk, because foreshortening near the limb hampers any type of magnetic modeling. The time input information defines a time series,

$$t_i = t_{\text{start}} + i \times t_{\text{cad}}, i = 1, \dots, n_t, \tag{1}$$

where the number n_t of time frames amounts to

$$n_t = \frac{t_{\text{dur}}}{t_{\text{cad}}},\tag{2}$$

for which magnetic solutions are computed. For flare events we typically use a cadence of $t_{\rm cad} = 6$ minutes (down to 1 minute), a duration $t_{\rm dur} = \Delta t_{\rm flare} + 2t_{\rm margin}$ that corresponds to the flare duration $\Delta t_{\rm flare}$ augmented with a margin of $t_{\rm margin} = \pm 1.0$ hr before and after the flare event. For the study of the time evolution of an active region, for instance, we used a total duration of 5 days with a cadence of $t_{\rm cad} = 6$ minutes, which requires $n_t = 5 \times 24 \times 10 = 1200$ time steps (Figure 2).

The architecture of the VCA-NLFFF code entails sequential processing of the three major tasks to compute non-potential-field solutions for each single time step, but an arbitrary number of time steps can be simultaneously processed in parallel, since the code treats all data from each time step independently. The efficient mode of parallel processing allows us to compute results in real time, in principle for any time cadence, if a sufficient number of parallel runs is organized.

2.2. Heliographic Coordinates

The heliographic position of the center of the chosen FOV subimages is automatically updated from the change in heliographic longitude according to the differential rotation,

$$l(t) = l(t_{\text{start}}) + \frac{(t - t_{\text{start}})}{t_{\text{syn}}} \times 360^{\circ}, \tag{3}$$

with the synodic period being $t_{\rm syn}(b=0)=27.2753$ days. The absolute accuracy of the time-dependent heliographic coordinates is not critical in the accuracy and continuity of the time-dependent free energy $E_{\rm free}(t)$, as long as the chosen FOV has weak magnetic fields at the boundaries. The relative accuracy among different wavelengths is given by the instrument cadence, which is $\Delta t_{\rm cad}=12$ s for AIA data from SDO. Based on this input, the code generates first a catalog with n_t time entries that contain the times t_i and the time-dependent heliographic positions $[l_i, b_i]=[l(t_i), b(t_i)]$ for each time step.

All computations are carried out in a Cartesian coordinate system [x, y, z] with the origin of the coordinate system at Sun center and z being aligned with the observer's line-of-sight. All solar images are required to have the solar north–south direction co-aligned with the y-axis (which is provided in the level-1.5 data after running AIA_PREP). The heliographic positions [l, b] are transformed into Cartesian coordinates [x, y] by taking the sinusoidal (annual) variation of the latitude $b_0(t)$ of the Sun center into account,

$$b_0(t) = 7.24 \sin[2\pi(t - t_0)],$$
 (4)

where t_0 is the time when the tilt angle of the solar axis is zero $(b_0 = 0)$, when the solar equator coincides with the east—west axis, which occurs on June 6. From this we can calculate the Cartesian coordinates $[x_0, y_0]$ of a target with heliographic

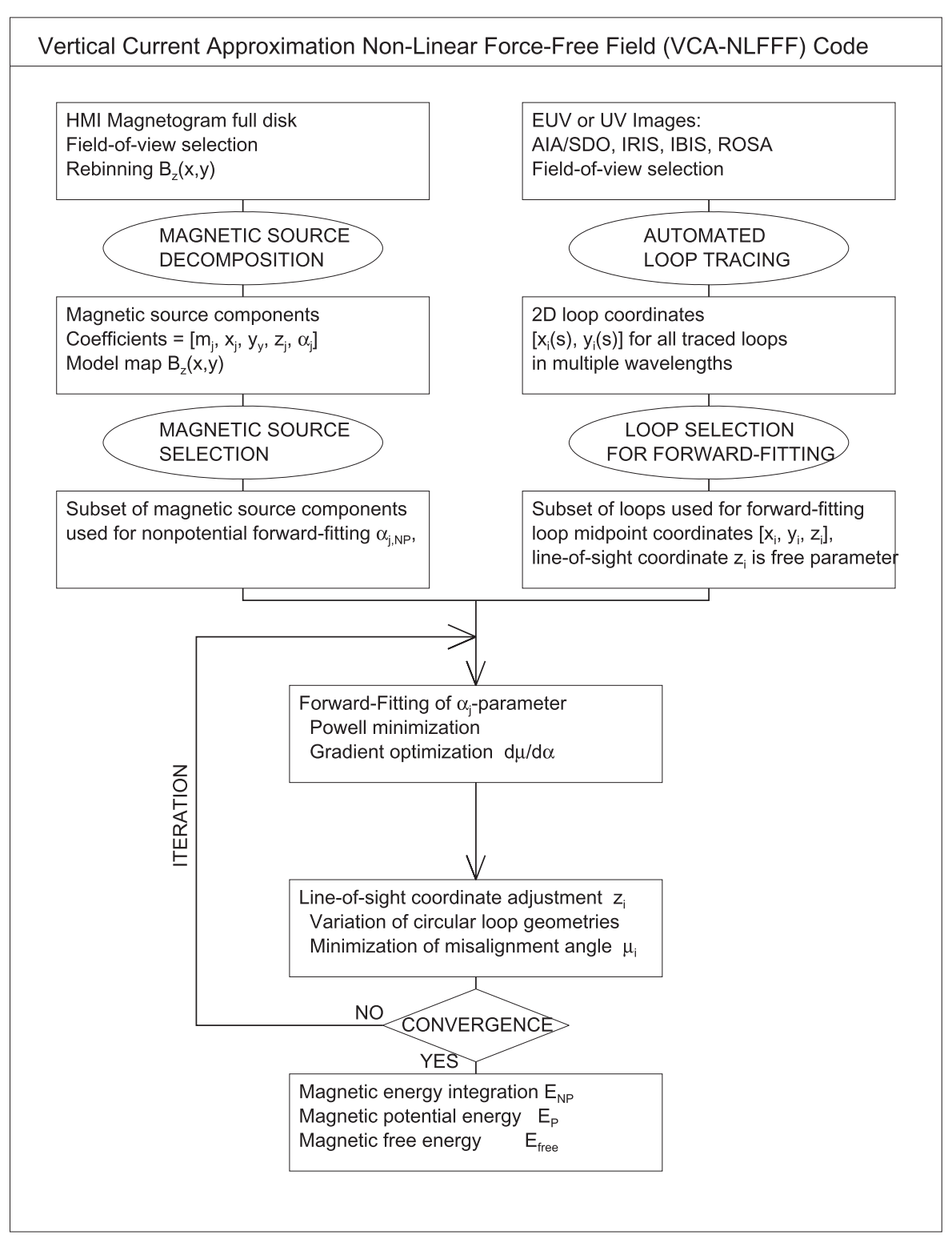


Figure 1. Flow chart of the VCA-NLFFF code, which includes a decomposition of the magnetic data (top left), automated tracing of curvi-linear structures (top right), and forward fitting using both data sets (bottom half; adapted from Aschwanden et al. 2014a).

coordinates [l, b] by,

$$x_0 = \sin\left(l\frac{\pi}{180^\circ}\right)\cos\left(b\frac{\pi}{180^\circ}\right),\tag{5}$$

$$y_0 = \sin \left[(b - b_0) \frac{\pi}{180^{\circ}} \right].$$
 (6)

The left and right-hand side of a chosen square FOV with length FOV has then the Cartesian coordinates $x_1 = x_0 - \text{FOV}/2$ and $x_2 = x_0 + \text{FOV}/2$, while the bottom and top boundaries are $y_1 = y_0 - \text{FOV}/2$ and $y_2 = y_0 + \text{FOV}/2$. The relationship between the Cartesian and heliographic coordinate systems is illustrated in Figure 2 for a time sequence

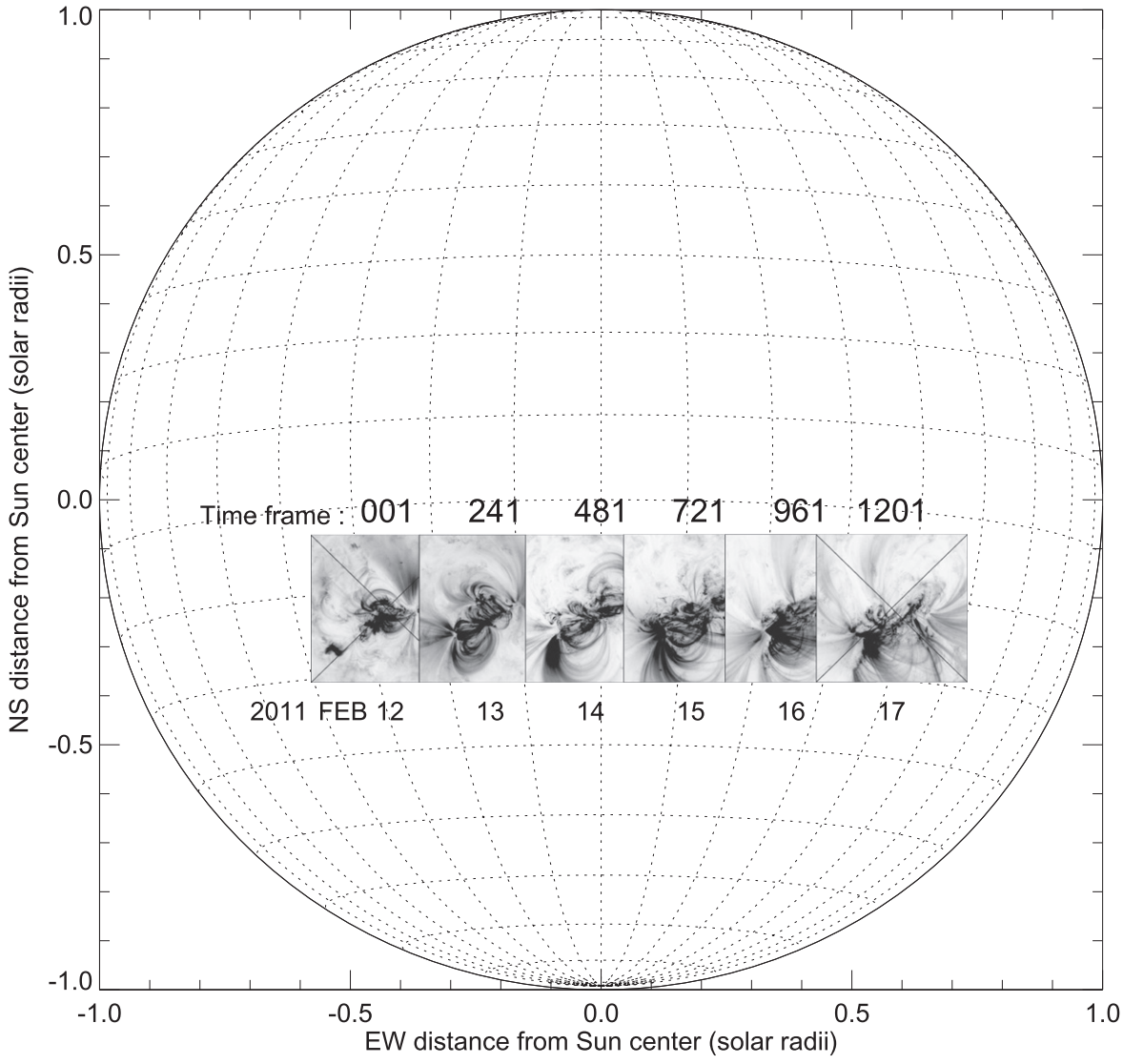


Figure 2. Example of a time grid with 1200 steps is shown for AR 11158 on 2011 February 12 through 17, showing the time-dependent FOV at the beginning of each day (00:00 UT). The *x*-axis and *y*-axis indicate the Cartesian coordinate system, while a grid of longitudes and latitudes with 10° spacing illustrates the heliographic coordinate system. The heliographic position of a selected time frame refers to the center of the subimage (indicated with a diagonal cross in the first and last frame).

of EUV subimages that follow the track of NOAA active region 11158.

2.3. Wavelength Selection

The data input requires a minimum of a line-of-sight magnetogram and at least one EUV (or UV) image that shows curvi-linear features, such as coronal loops or chromospheric fibrils. However, an arbitrary large number of EUV (or UV) images can be supplied for each time step. The present version of the code deals with HMI/SDO magnetograms and EUV and UV images from AIA/SDO (94, 131, 171, 193, 211, 304, 335, 1600 Å), from the *Interface Region Imaging Spectrograph (IRIS*; De Pontieu et al. 2014) slit-jaw images (1400, 2796, 2832 Å), from the Interferometric Bidimensional Spectrometer (IBIS; Cavallini 2006; 8542 Å), or from the Rapid Oscillations in the Solar Atmosphere (ROSA; Jess et al. 2010) instrument (6563 Å). In the present code version, up to eight different wavelengths from the same instrument are processed in a single run. We will subdivide the wavelengths chosen in each

instrument further by coronal (94, 131, 171, 193, 211, 335 Å) and chromospheric contributions (304, 1400, 1600, 1400, 2796, 2832, 6563, 8542 Å). A sample of such a multi-wavelength data set used in magnetic modeling with the VCA-NLFFF code is depicted in Figure 3, revealing loop structures in coronal wavelengths as well as fibrils and moss in chromospheric wavelengths, which pose an intricate problem for automated tracing of magnetic field-aligned curvi-linear features.

The data input in the VCA-NLFFF code is organized in two ways, either by reading the data FITS files from a specified directory on the local computer, or by searching level-1.5 data from local disk cache, or remotely from the official *SDO* and *IRIS* data archives (at Stanford University and Lockheed Martin). AIA/*SDO*, HMI/*SDO*, and *IRIS* level-1.5 data are available in form of FITS files with all necessary pointing information, while other data (e.g., from IBIS and ROSA) need to be prepared with a minimal FITS header that contains the pointing information (specified with the FITS descriptors

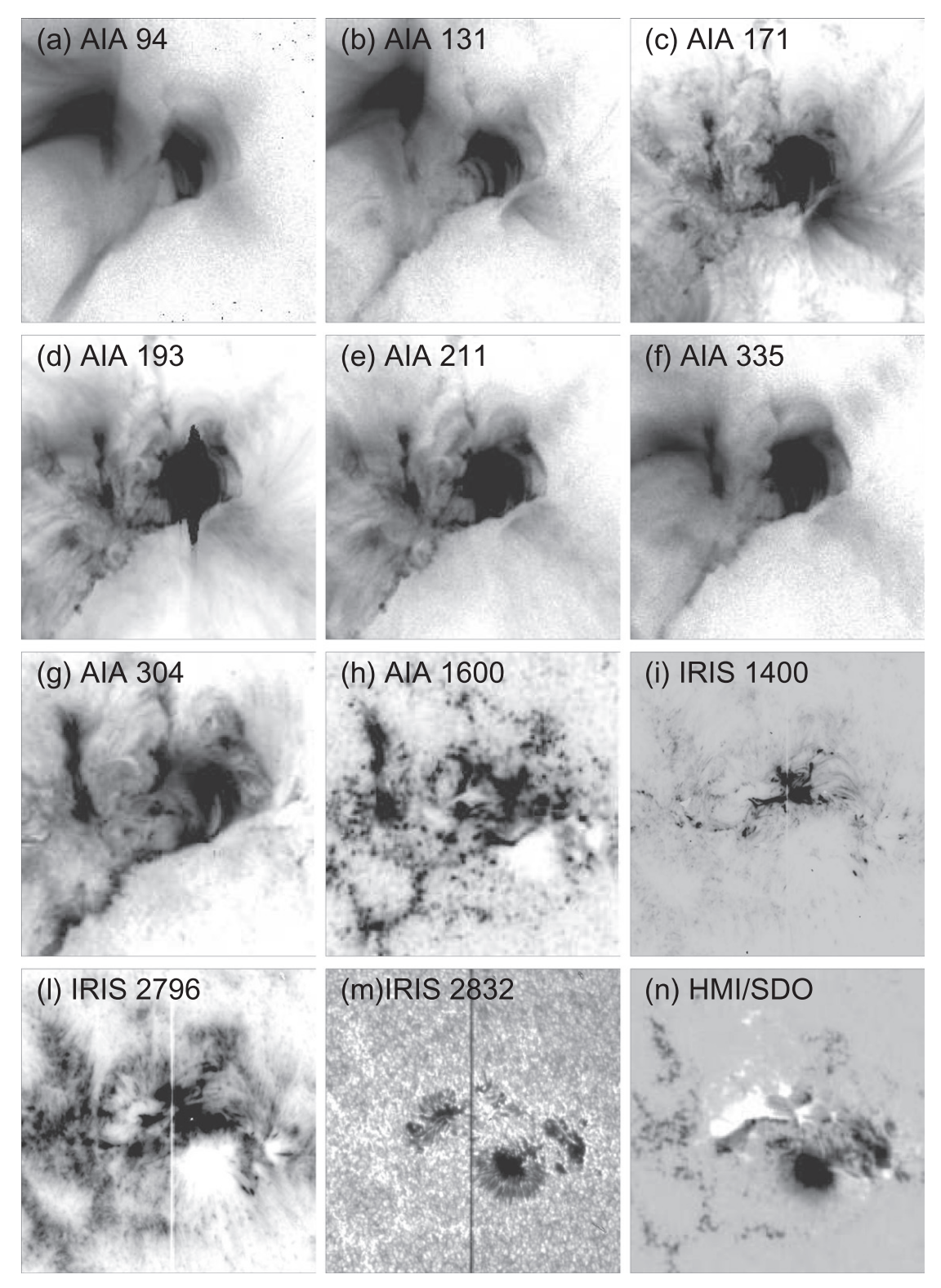


Figure 3. Example of an image set that is used for modeling with the VCA-NLFFF code for a single time step, containing subimages in eight AIA/SDO wavelengths (panels (a)–(h)), three *IRIS* wavelengths (panels (i)–(m)), and the corresponding HMI/SDO magnetogram (panel (n)). This data set was observed on 2014 March 29, 18:17 UT with AIA, and at 17:35 UT with *IRIS*, shown for a FOV of 0.1 solar radii, centered at heliographic position N10W33. The grayscale of the images is inverted (panels (a)–(j)), except for *IRIS* 2832 and HMI (panels (m), (n)), on a logarithmic intensity scale for AIA images (panels (a)–(g)), and on a linear scale for the others (panels (h)–(n)). The AIA images show a compact post-flare loop arcade, while *IRIS* images reveal chromospheric features. CCD saturation is visible in the AIA 195 Å image (panel (d)).

Table 1

Data Selection Parameters and Adjustable Control Parameters of the VCA-NLFFF Forward-fitting Code Used in this Study

Task	Control parameter	Value		
Data selection	Instruments	HMI; AIA; IRIS; IBIS; ROSA		
	Spatial pixel size	0."5; 0."6; 0."16; 0."1; 0."1		
	Wavelengths	6173; [94,131,171,193,211,304,335,1600]; [1400,2796,2832]; 8542; 6563 Å		
	FOV	$FOV = 0.1,, 0.4R_{\odot}$		
Magnetic sources	Number of magnetic sources	$n_{\rm mag} = 30$		
	Width of fitted local maps	$w_{\rm mag} = 3 \text{ pixels}$		
	Depth range of buried charges	$d_{\rm mag}=20$ pixels		
	Rebinned pixel size	$\Delta x_{\text{mag}} = 3 \text{ pixels} = 1.75$		
Loop tracing	Maximum of traced structures	$n_{\rm struc} = 1000$		
	Lowpass filter	$n_{\rm sm1} = 1$ pixel		
	Highpass filter	$n_{\rm sm2} = n_{\rm sm1} + 2 = 3 \text{ pixels}$		
	Minimum loop length	$l_{\min} = 5$ pixels		
	Minimum loop curvature radius	$r_{\min} = 8 \text{ pixels}$		
	Field line step	$\Delta s = 0.002 R_{\odot}$		
	Threshold positive flux	$q_{\mathrm{thresh},1}=0$		
	Threshold positive filter flux	$q_{\mathrm{thresh},2}=0$		
	Proximity to magnetic sources	$d_{\rm prox} = 10$ source depths		
Forward-fitting	Misalignment angle limit	$\mu_0 = 20^{\circ}$		
	Minimum number of iterations	$n_{\rm iter,min} = 40$		
	Maximum number of iterations	$n_{\text{iter,max}} = 100$		
	Number loop segment positions	$n_{\text{seg}} = 9$		
	Maximum altitude	$h_{ m max}=0.2R_{\odot}$		
	α -parameter increment	$\Delta\alpha_0 = 1.0R_\odot^{-1}$		
	Isotropic current correction	$q_{\rm iso} = (\pi/2)^2 \approx 2.5$		

NAXISi, CDELT1i, CRVALi, CRPIXi, and CROTAi, i = 1, 2; see Thompson 2006).

2.4. Performance Test Data

The validity of the results obtained with the VCA-NLFFF code can most rigorously be tested with independent data from other NLFFF codes. The most suitable data set containing published results of potential, non-potential, and free energies has been computed with the weighted optimization NLFFF method (Wiegelmann 2004; Wiegelmann et al. 2006, 2008; Wiegelmann & Inhester 2010) by Xudong Sun for active region AR 11158 during 5 days (2011 February 12–17) with a cadence of 12 minutes, yielding 600 time steps for NLFFF comparisons (Aschwanden et al. 2014a). The corresponding VCA-NLFFF solutions are calculated for a time cadence of 6 minutes, yielding 1200 time steps (Figure 2).

We will use a second test data set of 11 *GOES* X-class flares with measurements of potential, non-potential, and free energies, computed by Xudong Sun using Wiegelmann's NLFFF method, with a 12 minute cadence during each flare time interval, providing 119 time steps for NLFFF comparisons (Aschwanden et al. 2014b).

A third test data set is used here from the 2014 March 29 GOES X-class X1.0 flare, the first X-class flare that was observed by IRIS, where we have simultaneous coverage with AIA and IRIS, so that magnetic energies based on wavelengths from the coronal as well as chromospheric regime can be compared, which was the topic of a previous study (Aschwanden 2015). In particular we will use this test data set for a parametric study of the control parameters operating in the VCA-NLFFF code (Section 5.6), as listed in Table 1.

A list of the observing times, time ranges, cadences, number of time steps, *GOES* class, heliographic position, NOAA active region number, and observing instruments of the three test data sets is compiled in Table 2.

3. THE POTENTIAL FIELD

3.1. Analytical Description

The simplest representation of a magnetic potential field that fulfills Maxwell's divergence-free condition ($\nabla \cdot \mathbf{B} = 0$) is a unipolar magnetic charge m that is buried below the solar surface (Aschwanden 2013a), defining a magnetic field $\mathbf{B}_m(\mathbf{x})$ that falls off with the square of the distance r_m ,

$$\boldsymbol{B}_{m}(\boldsymbol{x}) = B_{m} \left(\frac{d_{m}}{r_{m}}\right)^{2} \frac{\boldsymbol{r}_{m}}{r_{m}},\tag{7}$$

where B_m is the magnetic field strength at the solar surface above a buried magnetic charge, (x_m, y_m, z_m) is its subphotospheric position, d_m is the depth of the magnetic charge,

$$d_m = 1 - \sqrt{x_m^2 + y_m^2 + z_m^2}, (8)$$

and $\mathbf{r}_m = [x - x_m, y - y_m, z - z_m]$ is the vector between an arbitrary location $\mathbf{x} = (x, y, z)$ in the solar corona and the location (x_m, y_m, z_m) of the buried charge. We define a Cartesian coordinate system (x, y, z) with the origin at the Sun center and the direction z chosen along the line-of-sight from Earth to Sun center. The distance r_m from the magnetic charge is

$$r_m = \sqrt{(x - x_m)^2 + (y - y_m)^2 + (z - z_m)^2}$$
 (9)

SDO, IRIS

Flare Number	Start Time (UT)	Duration	Cadence NLFFF, AIA	Time Steps NLFFF, AIA	GOES Class	Heliographic Position	NOAA AR	Instrument
10–15	2011 Feb 12–17	5 days	12, 6 minutes	600, 1200	C1.0-X2.2	S20E27-W38	11158	SDO
12	2011 Feb 15, 00:44	2.4 hr	12, 6 minutes	12, 24	X2.2	S21W12	11158	SDO
37	2011 Mar 09, 22:13	2.3 hr	12, 6 minutes	11, 23	X1.5	N10W11	11166	SDO
66	2011 Sep 06, 21:12	2.3 hr	12, 6 minutes	11, 23	X2.1	N16W15	11283	SDO
67	2011 Sep 07, 21:32	2.3 hr	12, 6 minutes	6, 12	X1.8	N16W30	11283	SDO
147	2012 Mar 06, 23:02	2.7 hr	12, 6 minutes	13, 27	X5.4	N18E31	11429	SDO
148	2012 Mar 07, 00:05	2.4 hr	12, 6 minutes	12, 24	X5.4	N18E29	11430	SDO
220	2012 Jul 12, 14:37	3.9 hr	12, 6 minutes	19, 39	X1.4	S15W05	11520	SDO
344	2013 Nov 05, 21:07	2.2 hr	12, 6 minutes	11, 22	X3.3	S08E42	11890	SDO
349	2013 Nov 08, 03:20	2.2 hr	12, 6 minutes	11, 22	X1.1	S11E11	11890	SDO
351	2013 Nov 10, 04:08	2.2 hr	12, 6 minutes	11, 22	X1.1	S11W17	11890	SDO
384	2014 Jan 07, 17:04	3.0 hr	12, 6 minutes	15, 30	X1.2	S12E02	11944	SDO

Table 2

Data Sets Used in Performance Tests of the VCA-NLFFF code in this Study

Note. The flare number corresponds to a continuous numbering of M- and X-class flares since start of the *SDO* mission. The duration includes a time interval of ± 1 (or ± 0.5) hr before and after flares.

..., 13

X1.0

.... 6 minutes

The absolute value of the magnetic field $B_m(r_m)$ is a function of the radial distance r_m (with B_m and d_m being constants for a given magnetic charge),

2014 Mar 29, 17:05

592

$$B_m(r_m) = B_m \left(\frac{d_m}{r_m}\right)^2. \tag{10}$$

1.3 hr

We can generalize from a single magnetic charge to an arbitrary number $n_{\rm mag}$ of magnetic charges and represent the general magnetic field with a superposition of $n_{\rm mag}$ buried magnetic charges, so that the potential field can be represented by the superposition of $n_{\rm mag}$ fields \boldsymbol{B}_m from each magnetic charge $m=1,\ldots,n_{\rm mag}$,

$$\boldsymbol{B}(\boldsymbol{x}) = \sum_{m=1}^{n_{\text{mag}}} \boldsymbol{B}_{m}(\boldsymbol{x}) = \sum_{m=1}^{n_{\text{mag}}} B_{m} \left(\frac{d_{m}}{r_{m}}\right)^{2} \frac{r_{m}}{r_{m}}.$$
 (11)

An example of a unipolar charge with a radial magnetic field is a single sunspot (Figure 4, top panels), while a dipole field requires two magnetic charges with opposite magnetic polarity (Figure 4, second row). Typically, the magnetic field of an active region can be represented by a superposition of $n_{\rm mag} \approx 20{\text -}100$ unipolar magnetic sources, depending on the topological complexity of the magnetic field. Examples of magnetic models with $n_{\rm mag} = 10$ and $n_{\rm mag} = 100$ components are shown in Figure 4 also (Figure 4, third and bottom row panels).

A numerical algorithm that deconvolves a line-of-sight magnetogram $B_z(x, y, z_{\text{phot}})$ has to solve the task of inverting the four observables (B_z, ρ_m, z_m, w_m) into the four model parameters (B_m, x_m, y_m, z_m) for each magnetic charge, where B_z is the observed line-of-sight component of the magnetic field at the photosphere, ρ_m is the apparent distance of a magnetic source from Sun center, $z_m = \sqrt{1 - \rho_m^2}$ is the distance from the plane-of-sky (through Sun center), w_m is the FWHM of the magnetic source, B_m is the magnetic field of the magnetic charge m at the solar surface, and (x_m, y_m, z_m) are the 3D coordinates of a buried magnetic charge. The geometric parameters are defined in Figure 5. An analytical derivation

of the inversion of an observed line-of-sight magnetogram into the model parameters of the VCA-NLFFF code is described in Appendix A of Aschwanden et al. (2012). Starting from an approximate initial guess of the aspect angle α , since $\tan(\alpha) = (\rho_m/z_m) \approx (\rho_p/z_p)$, we obtain an accurate value by iterating the following sequence of equations a few times,

N10W33

12017

$$\alpha \approx \arctan(\rho_p/z_p)$$

$$\beta_p = \arctan[(\sqrt{9 + 8 \tan^2 \alpha} - 3)/4 \tan \alpha]$$

$$B_m = B_z/[\cos^2 \beta_p \cos(\alpha - \beta_p)]$$

$$\beta_2 = \arccos[((\cos \beta_p)^3/2)^{1/3}]$$

$$d_m = w/[\tan \beta_2 \cos \alpha (1 - 0.1\alpha)]$$

$$r_m = (1 - d_m)$$

$$\rho_m = \rho_p - d_m \sin(\alpha - \beta_p)/\cos \beta_p$$

$$z_m = \sqrt{r_m^2 - \rho_m^2}$$

$$x_m = \rho_m \cos \gamma$$

$$y_m = \rho_m \sin \gamma$$

$$\alpha = \arctan(\rho_m/z_m).$$
(12)

This decomposition procedure of a line-of-sight magnetogram $B_z(x, y)$ into a finite number $n_{\rm mag}$ of unipolar magnetic charges, each one parameterized with four parameters (B_m, x_m, y_m, z_m) , allows us to compute the 3D potential-field vectors $\boldsymbol{B}(x)$ at any location of a 3D computation box above the photosphere (with $r = \sqrt{(x^2 + y^2 + z^2)} > 1$ solar radius), where the line-of-sight component $B_z(x, y)$ corresponding to the magnetogram is just one special component at the curved solar surface, while the transverse components $B_x(x, y)$ and $B_y(x, y)$ are defined by the same potential model with Equation (11). This algorithm is able to deconvolve magnetograms out to longitudes of $l \lesssim 80^\circ$ with an accuracy of $q_e = E_{\rm model}/E_{\rm obs} = 1.000 \pm 0.024$ in the conservation of the potential energy for a dipolar configuration (see Figure 21 in Aschwanden et al. 2014b), but we limit the application to $l \lesssim 45^\circ$ for general magnetograms.

The numerical VCA-NLFFF code contains four control parameters (Table 1): the number of magnetic charges n_{mag} , the

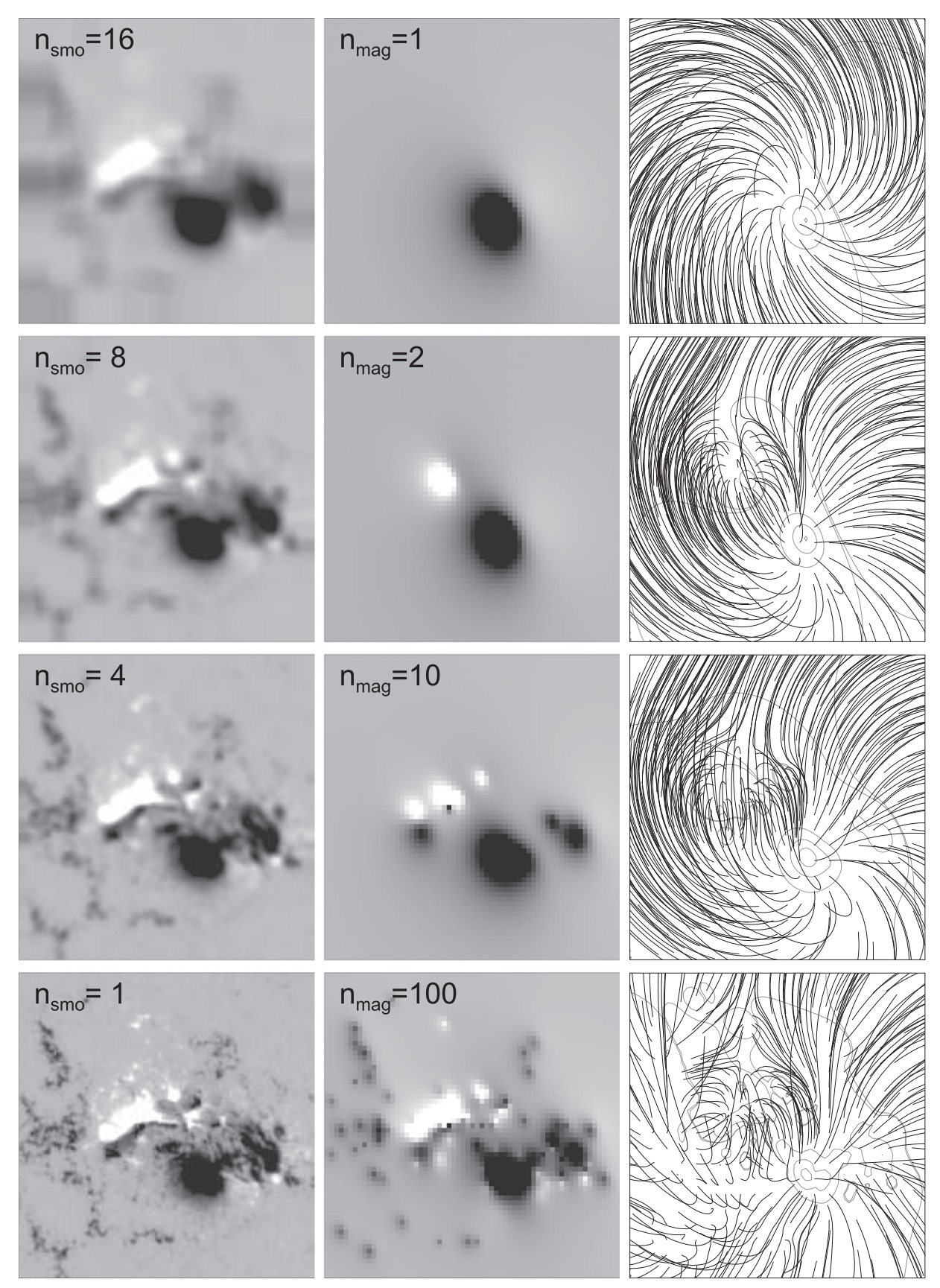


Figure 4. Decomposition of a line-of-sight magnetogram $B_z(x, y)$ (bottom left) into a finite number of $n_{\text{mag}} = 1, 2, 10$, or 100 magnetic sources (middle column) is shown with the corresponding potential field (field lines in right column), overlaid on the (gray) contours of the magnetogram. For comparison, a spatial smoothing of the magnetogram is shown also, with smoothing boxcars of $n_{\text{smo}} = 4, 8$, and 16 pixels of the original HMI resolution (panels in left column).

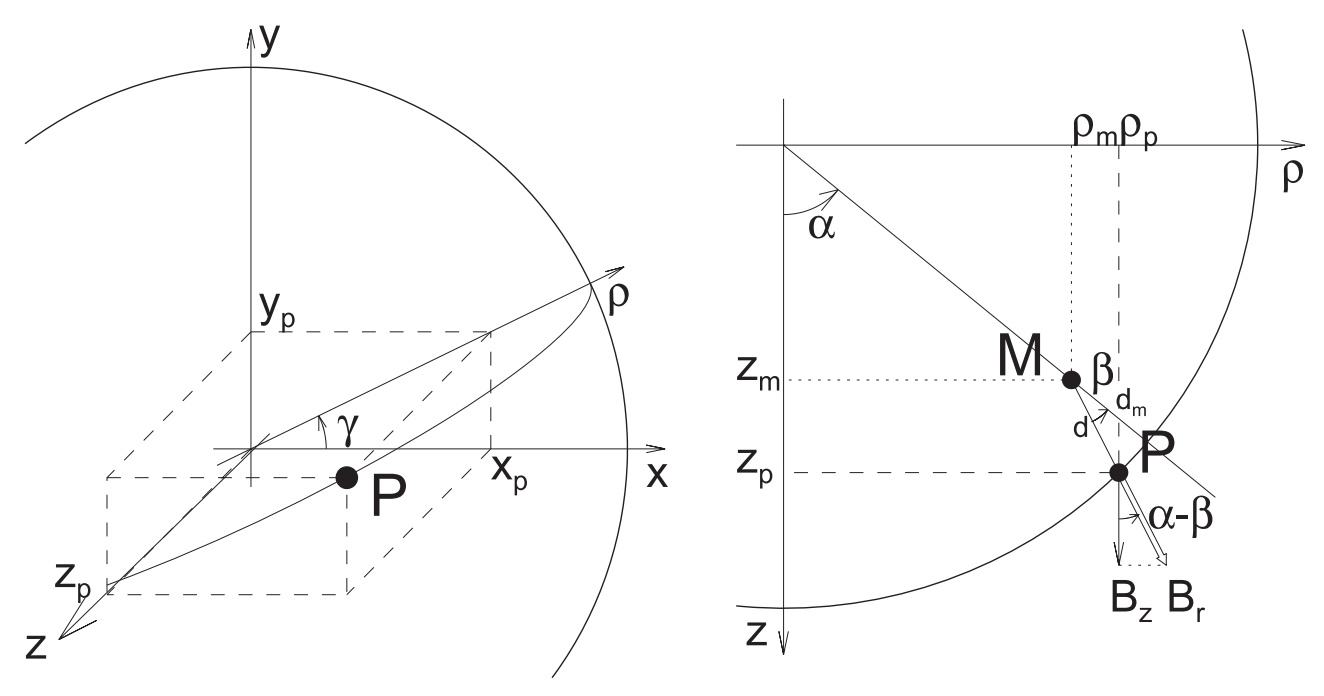


Figure 5. Three-dimensional geometry of a point source $P = (x_p, y_p, z_p)$ in a Cartesian coordinate system is shown (left), with the *z*-axis aligned to the line-of-sight from Earth to Sun center. The plane through the line-of-sight axis and the point source P has a position angle γ in the plane-of-sky with respect to the *x*-axis and defines the direction of the axis ρ . The geometry of a line-of-sight magnetic field component B_z is shown in the (z, ρ) -plane on the right-hand side. A magnetic point charge M is buried at position (z_m, ρ_m) and has an aspect angle α to the line-of-sight. The radial component B_z is observed on the solar surface at location P and has an inclination angle of β to the local vertical above the magnetic point charge M. The line-of-sight component B_z of the magnetic field has an angle $(\alpha - \beta)$ to the radial magnetic field component B_z . See details in Appendix A in Aschwanden et al. (2012)).

width $w_{\rm mag}$ of a local map where the magnetic source components are deconvolved, the depth range $d_{\rm mag}$ in which magnetic charges are buried, and the degradation scale $n_{\rm rebin}$ of magnetogram smoothing. While the number $n_{\rm mag}$ of magnetic charges is a free parameter that can be selected by the user, the other control parameters were optimized for robustness of results using HMI magnetograms (with a pixel size of 0."5), and are set to the constants $w_{\rm mag} = 3$ pixels, $d_{\rm mag} = 20$ pixels, and $n_{\rm rebin} = 3$ pixels. The robustness of the results as a function of these control parameters is also shown in the parameter study in Figure 15 of Aschwanden et al. (2012).

3.2. Performance Test of Potential Energy

In a first performance test we compare the potential energies $E_{\rm pot}$ that have been computed simultaneously with the weighted optimization NLFFF code (Wiegelmann 2004; Wiegelmann et al. 2006, 2008; Wiegelmann & Inhester 2010), which we briefly call W-NLFFF in the following, and with our VCA-NLFFF code. The potential energy of an active region or flare is defined here as the volume integral of the magnetic potential energy integrated over the entire 3D computation box, with the volume defined by the chosen FOV in x and y-direction, i.e., $[x_1, x_2]$ and $[y_1, y_2]$, while the z-range covers the height range bound by the photosphere, $z_1(x, y) = \sqrt{(1 - x^2 - y^2)}$, and a curved surface at a height of $h_{\rm max} = 0.2$ solar radii, i.e., $z_2(x, y) = \sqrt{([1 + h_{\rm max}]^2 - x^2 - y^2)}$,

$$E_{\text{pot}} = \int_{x_1}^{x_2} \int_{y_1}^{y_2} \int_{z_1(x,y)}^{z_2(x,y)} \frac{B_{\text{pot}}^2(x, y, z)}{8\pi} \, dx \, dy \, dz.$$
 (13)

Note that the total magnetic energy density $B^2/8\pi = (B_x^2 + B_y^2 + B_z^2)/8\pi$ includes both the line-of-sight component

 B_z and the two transverse components B_x and B_y . The transverse components are much less accurately known than the line-of-sight component, by a factor of about 20 for HMI (Hoeksema et al. 2014). The observed transverse components enter the energy estimate with the W-NLFFF method, while they are self-consistently determined from the potential-field model with the VCA-NLFFF model, and thus have a similar accuracy as the line-of-sight component in the VCA-NLFFF model

The total potential (or non-potential) energy is found in a range of $E_{\rm pot} \approx 10^{32} - 10^{33} \, {\rm erg}$ for the active region NOAA 11158, and increases to $E_{\rm pot}\approx 10^{33}$ – 10^{34} erg for X-class flares. In Figure 6, we show the potential energies $E_{\rm pot}^{\rm VCA}$ measured with the VCA-NLFFF code versus the potential energies $E_{
m pot}^W$ measured with the W-NLFFF code. Both codes integrate nearly over the same volume (although the W-NLFFF code does not take the sphericity of the solar surface into account), but the exact boundaries are not critical since most of the potential energy comes from the central sunspot in the FOV area of an active region or flare. The scatter plots in Figure 6 show a potential energy ratio of $q_{E, \text{pot}} = 1.22 \pm 0.39$ for 600 measurements of AR 11158 during 5 days observed on 2011 February 12-17 (Aschwanden et al. 2014a), and $q_{E, \text{pot}} = 0.76 \pm 0.18$ for 119 measurements of 11 X-class flares observed during 2011-2014 (Aschwanden et al. 2014a). Thus the average accuracy of the two NLFFF methods agrees within ≈25% for the total potential energy. The accuracy is similar for the non-potential energies (Figure 6, middle panels), and for the free energy (Figure 6, bottom panels). This accuracy is similar to the differences of 12%-24% in the potential energy that was

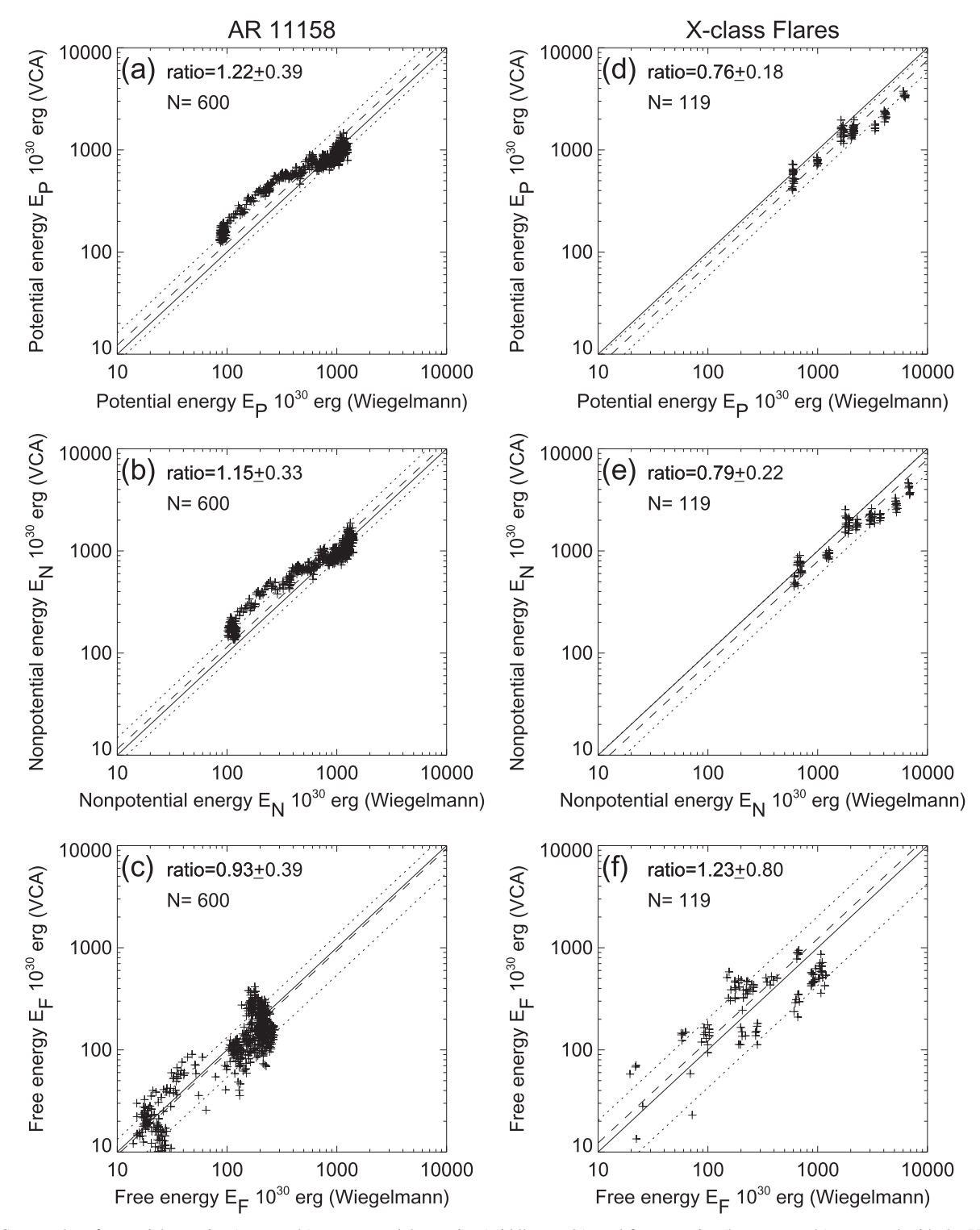


Figure 6. Scatter plot of potential energies (top panels), non-potential energies (middle panels), and free energies (bottom panels) measured with the VCA-NLFFF code (*y*-axis) and the Wiegelmann-NLFFF code (*x*-axis) for 600 time steps of AR 11158 observed during 5 days (left panels), and for 11 X-class flares (right panels). The diagonal lines indicate equality (solid lines), mean ratios (dashed lines), and standard deviations (dotted lines).

found among different NLFFF codes for NOAA active region 10978 (DeRosa et al. 2015).

There are three effects that mostly influence the accuracy of the potential-field measurement, namely, the spatial resolution of the magnetogram, the finite number of magnetic source components in the magnetic model, and the asymmetry of sunspots. The spatial resolution of a HMI magnetogram is given by the pixel size of 0.75, which is further downgraded to $n_{\rm rebin}=3$ pixels in our VCA-NLFFF code, which prevents a fragmentation into too many small magnetic elements that do not significantly contribute to the total energy. We can measure this effect by calculating the ratio $q_{E,{\rm rebin}}$ of potential energies from both the magnetogram with the original full resolution of 0.75 and the rebinned magnetogram with 1.75 used in the

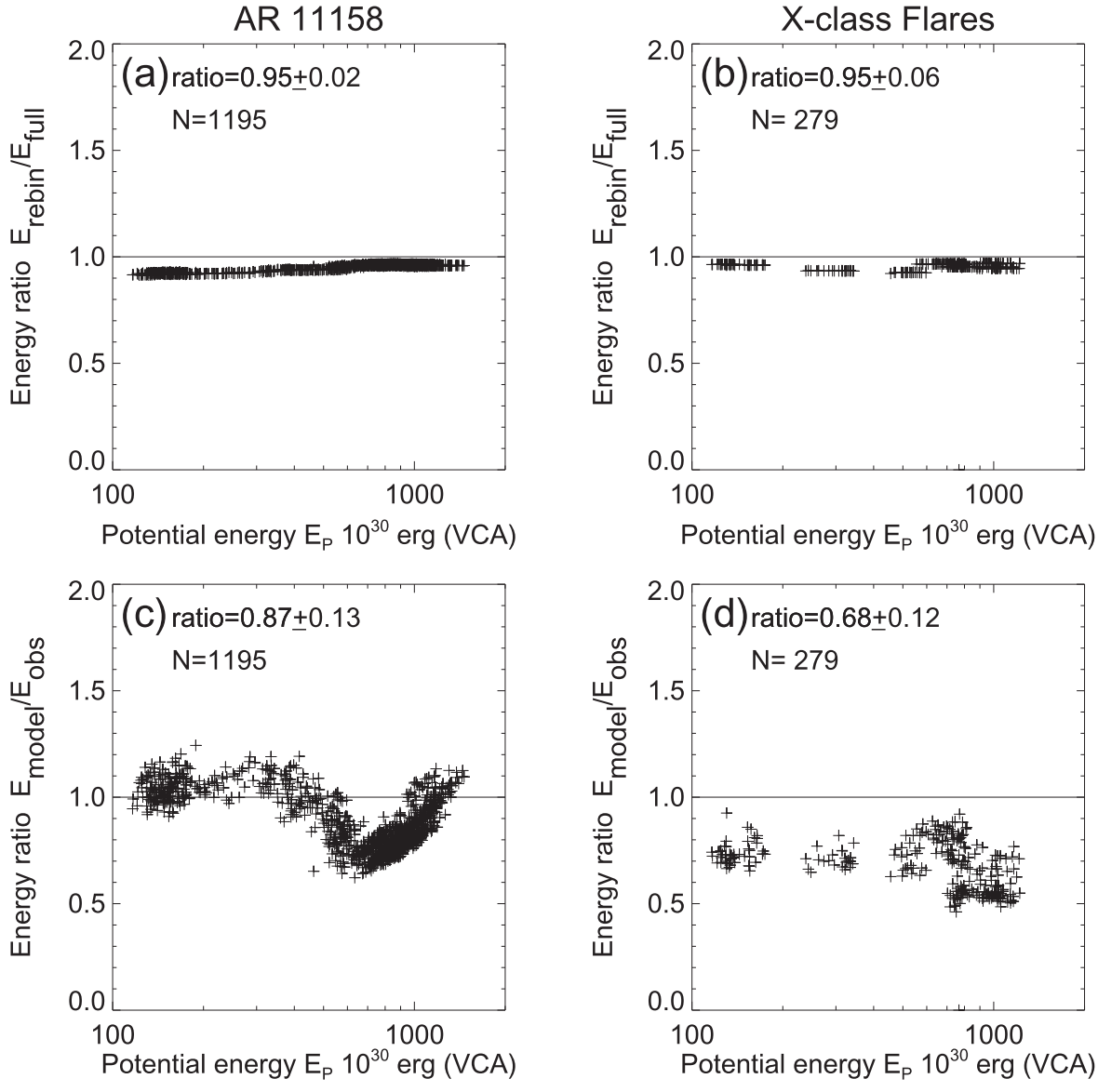


Figure 7. Test of conservation of the potential energy due to rebinning of the HMI magnetograms from 0.75 to 1.75 (top panels) and due to the model representation of the magnetogram with a finite number of (typically $n_{\text{mag}} = 30$) magnetic source components (bottom panels), for 1195 time steps of NOAA active region 11158 during 2011 February 12–17 (left panels), and 279 time steps of 11 X-class flares (right panels).

decomposition of magnetic sources,

$$q_{E,\text{rebin}} = \frac{\iint B_{z,\text{rebin}}^2(x, y) \, dx \, dy}{\iint B_{z,\text{full}}^2(x, y) \, dx \, dy}.$$
 (14)

We find a ratio of $q_{E,{\rm rebin}}=0.95\pm0.02$ for the potential energies due to rebinning, for the 1195 time steps of AR 11158 (Figure 7, top left panel), and $q_{E,{\rm rebin}}=0.95\pm0.06$ for 11 X-class flares (Figure 7, top right panel). Thus the degradation of the magnetogram introduces only an underestimate of $\approx 5\%$ in the potential or non-potential energy.

Similarly, we can investigate the effect of the finite number $n_{\rm mag}$ of magnetic source components, by calculating the potential energies from the line-of-sight magnetogram, and by comparing with the potential energies obtained from the

model (with $n_{\text{mag}} \approx 30$ source components),

$$q_{E,\text{model}} = \frac{\int \int B_{z,\text{model}}^2(x, y) \, dx \, dy}{\int \int B_{z,\text{obs}}^2(x, y) \, dx \, dy}.$$
 (15)

We find a ratio of $q_{E, \rm model} = 0.87 \pm 0.13$ for the potential energies, using a model with 30 magnetic sources, for the 1195 time steps of AR 11158 (Figure 7, bottom left panel), and $q_{E, \rm model} = 0.68 \pm 0.12$ for 11 X-class flares (Figure 7, bottom right panel). Thus the model representation with ≈ 30 magnetic source components leads to an average underestimate of about 13% for magnetic energies in active regions, and up to 32% for the largest flares. The optimization NLFFF code of Wiegelmann is found to have a similar degree of uncertainty, based on the ratio of the total potential energy between the model and

observed data, i.e., $q_{E, \rm model} = 1.12$ –1.24 (see ratio E/E_0 in Table 2 of DeRosa et al. 2015).

Further testing revealed that the highest accuracy is not necessarily controlled by the number of magnetic source components, although this is true as a statistical trend. Ultimate accuracy can be achieved when the model parameterization matches the observed magnetic field distribution, which is fulfilled to the highest degree for sunspots or magnetic sources with spherical symmetry, due to the spherical symmetry of the model definition of vertical currents in the VCA-NLFFF method (Equation (11)). In contrast, asymmetric sunspots require a deconvolution into secondary source components, which generally fit the tails of an asymmetric magnetic field distribution less accurately than the primary central source at a local peak in the magnetogram.

4. AUTOMATED LOOP TRACING

4.1. General Description

The second major task of the VCA-NLFFF code is the automated tracing of loop coordinates [x(s), y(s)] (as a function of the loop length coordinate s) in a coronal or chromospheric image, observed in EUV, UV, optical, or $H\alpha$ wavelengths. The underlying principle of this task corresponds to convert a two-dimensional (2D) brightness image (x,y) into a set of one-dimensional (1D) curvi-linear structures [x(s), y(s)]. Although there exist a number of software codes that aim to perform the task of automated pattern recognition (e.g., see image segmentation methods in Gonzalez & Woods 2008), or an application of a union-finding algorithm in Jing et al. (2011), it is our experience that none of the standard methods yields satisfactory results for solar data, and thus we developed a customized code that is optimized for automated detection of curvi-linear features with relatively large curvature radii (compared with the width of a loop structure) observed in solar high-resolution images.

In an initial study, five different numerical codes, designed for automated tracing of coronal loops in Transition Region And Coronal Explorer images, were quantitatively compared (Aschwanden et al. 2008), including: (i) the orientedconnectivity method, (ii) the dynamic aperture-based loop segmentation method, (iii) the unbiased detection of curvilinear structures code, (iv) the oriented-direction method, and the (v) ridge detection by automated scaling method. One scientific result of this study was that the size distribution of automatically detected loops follows a cumulative powerlaw distribution $N(>L) \propto L^{-\beta}$ with $\beta \approx 2.0$ –3.2, which indicates a scale-free process that determines the distribution function of coronal loop segments. One of the original five codes was developed further, a prototype based on the method of Oriented Coronal Curved Loop Tracing (OCCULT-1), which approached an accuracy that was matching visual perception of "hand-traced" loops (Aschwanden 2010). An improved code (OCCULT-2) includes a second-order extrapolation technique (Figure 8) for tracing of curvi-linear features (Aschwanden et al. 2013b), permitting extended applications to AIA images, to chromospheric H α images, as well as applications to images in biophysics. While AIA/SDO images have a pixel size of 0."6, the automated loop tracing was also extended to higher spatial resolution, to images with pixel sizes corresponding to 0".16 (IRIS) and 0".1 (IBIS, ROSA; (M. J. Aschwanden et al. 2016, in preparation).

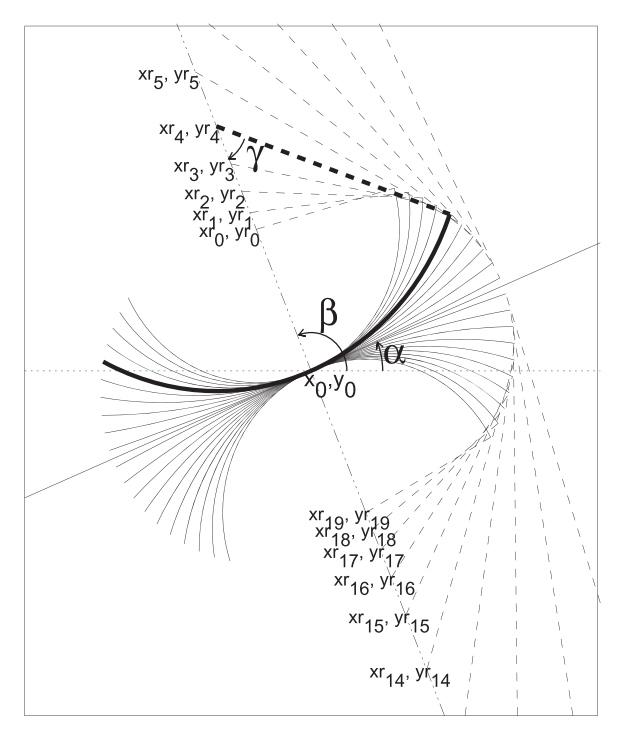


Figure 8. Geometry of automated curvi-linear feature tracking is shown, starting at a local flux maximum location (x_0, y_0) , where the linear direction of the local ridge is measured (angle α) and a set of circular segments within a range of curvature radii is fitted to the local ridge (thick linestyle). The locations (xr_i, yr_i) , i = 0, ..., 19 mark the centers of the curvature radii (Aschwanden et al. 2013b).

The analytical description of the OCCULT-2 code is given in Appendix A.1 of Aschwanden (2013a). The Interactive Data Language (IDL) source code is available in the Solar SoftWare (SSW), see the IDL procedure *LOOPTRACING–AUTO4.PRO.*¹

We briefly summarize the numerical algorithm and the control parameters that can affect the results (see also Table 1). The first step is the background subtraction, which can be quantified by a minimum level in the original intensity image $(q_{\text{thresh},1})$, as well as by a minimum level in the bipass-filtered image $(q_{\text{thresh},2})$. A bipass-filtered image is then created from a lowpass filter $I_{\text{low}}(x, y)$ (i.e., smoothing with a boxcar of n_{sm1} pixels) and a highpass filter $I_{\text{high}}(x, y)$ (i.e., smoothing with a boxcar of $n_{\text{sm2}} = n_{\text{sm1}} + 2$), while the bipass-filter image $\Delta I(x, y)$ is the difference between the two filters,

$$\Delta I(x, y) = I_{\text{high}}(x, y) - I_{\text{low}}(x, y). \tag{16}$$

We find that a lowpass filter with $n_{\rm sm1}=1$ and a highpass filter with $n_{\rm sm2}=n_{\rm sm1}+2=3$ pixels yields best results for most AIA images (Aschwanden et al. 2013b). The lowpass filter eliminates large-scale variations in the background, while the highpass filter eliminates random data noise. For noisy images, a somewhat higher value is recommended, such as $n_{\rm sm1}=3$ and $n_{\rm sm2}=n_{\rm sm1}+2=5$. The OCCULT-2 algorithm traces individual curvi-linear structures by finding first the location (x_1, y_1) of the absolute intensity maximum in the image $\Delta I(x, y)$, then measures the direction from the first derivative dy/dx $(x=x_1, y=y_1)$ of the ridge that passes true the flux maximum location (x_1, y_1) , as well as the curvature radius from

¹ A tutorial is available at the website http://www.lmsal.com/~aschwand/software/tracing_tutorial1.html.

the second derivative d^2y/dx^2 ($x = x_1, y = y_1$) (see geometric diagram in Figure 8), and traces the direction of the ridge pixel by pixel, until the end of the segment traced in forward direction reaches a negative flux (in the bipass-filtered image). The tracing is then also carried out in backward direction, in order to find the other end of the loop segment, yielding the coordinates [x(s), y(s)] of the entire traced loop as a function of the loop length coordinate s. The pixels that are located within a half width $(w_{half} = n_{sm2}/2 - 1)$ of the ridge coordinates [x(s), y(s)] are then erased and the residual image serves as input for tracing of the second structure, starting with next flux maximum (x_2, y_2) , and repeating the same steps to find the coordinates of the second brightest loop. The algorithm has nine control parameters (Table 1), which includes the maximum number of traced structures n_{struc} per wavelength, the lowpass filter n_{sm1} , the highpass filter $n_{\text{sm2}} = n_{\text{sm1}} + 2$, the minimum accepted loop length l_{\min} , the minimum allowed curvature radius r_{\min} , the field line step Δs along the (projected) loop coordinate, the flux threshold $q_{\text{thresh}1}$ in units of the median value of positive fluxes in the original image), the filter flux threshold q_{thresh} (also in units of the median value in the positive bipass-filtered fluxes), and a maximum proximity distance d_{prox} from the location of the next-located magnetic source. An additional parameter in the original code is $n_{\rm gap}$, which allowed to skip segments with negative bipassfiltered fluxes, but is set to $n_{gap} = 0$ in the current version of the code.

4.2. Numerical Examples

Examples of bipass-filtered images of all AIA and *IRIS* (slit-jaw) wavelengths are shown in Figure 9, which correspond to the observed original images shown in Figure 3, while the corresponding automated loop tracings are shown in Figure 10, sampled for a minimum loop length of $l_{\rm min} \geqslant 5$ pixels.

A few special features of the loop tracing code applied to solar data include the elimination of curvi-linear artifacts resulting from the boundaries of image portions with saturated fluxes or pixel bleeding (occurring in CCDs, see AIA 171 and 193 in Figures 9(c) and (d)), as well as the elimination of strictly horizontal and vertical features, that result from edges of incomplete image data, vignetting, or slit markers (especially in slit-jaw images from *IRIS*, see Figure 9). Scanning through thousands of images we find many other curvi-linear features that appear not to be aligned with the magnetic field, which are eliminated by restricting the maximum allowed misalignment angle μ_2 iteratively to smaller values in the forward-fitting algorithm of the VCA-NLFFF code.

5. THE NONLINEAR FORCE-FREE FIELD

5.1. Analytical Description

A non-potential field can be constructed by introducing a vertical current above each magnetic charge, which introduces a helical twist about the vertical axis (e.g., Figure 4, top right panel). There is an exact analytical solution for a straight uniformly twisted flux tube (e.g., Priest 1982), which can be generalized to the 3D spherical coordinates of a vertical flux tube that expands in cross-section according to the divergence-free and force-free condition and is accurate to second-order of the force-free α -parameter (Aschwanden 2013a). This vertical-

current approximation can be expressed by a radial potential-field component $B_r(r, \theta)$ and an azimuthal non-potential-field component $B_{\varphi}(r, \theta)$ in spherical coordinates (r, φ, ϑ) ,

$$B_r(r,\theta) = B_0 \left(\frac{d^2}{r^2}\right) \frac{1}{(1+b^2r^2\sin^2\theta)},\tag{17}$$

$$B_{\varphi}(r,\,\theta) = B_0 \left(\frac{d^2}{r^2}\right) \frac{br\sin\theta}{(1+b^2r^2\sin^2\theta)},$$
 (18)

$$B_{\theta}(r,\,\theta)\approx 0,$$
 (19)

$$\alpha(r,\theta) \approx \frac{2b\cos\theta}{(1+b^2r^2\sin^2\theta)}.$$
 (20)

$$b = \frac{2\pi n_{\text{twist}}}{l},\tag{21}$$

where $\alpha(r, \theta)$, generally known as the force-free α -parameter, is related to the parameter b that expresses the number n_{twist} of helical turns over the loop length l. The non-potential field of each magnetic charge $m=1,\ldots,n_{\rm mag}$ can be described with this approximation, and the associated field components B_r and B_{φ} have to be transformed into a common Cartesian coordinate system $\mathbf{B}_m^{\rm np}(\mathbf{x})$, and can then be added in linear superposition,

$$\boldsymbol{B}^{\mathrm{np}}(\boldsymbol{x}) = \sum_{m=1}^{n_{\mathrm{mag}}} \boldsymbol{B}_{m}^{\mathrm{np}}(\boldsymbol{x}), \tag{22}$$

which still fulfills the divergence-freeness and force-freeness to second-order accuracy (Aschwanden 2013a). This way we have a space-filling non-potential-field solution that is parameterized by five variables (B_m , x_m , y_m , z_m , α_m) for each magnetic charge $m=1,...,n_{\rm mag}$, where of the first four variables are already determined from the potential-field solution. From this parameterization we obtain directly a positively defined expression for the free energy $E_{\rm free}$ (Aschwanden 2013b), which is the difference between the non-potential field $E_{\rm NP}$ and the potential-field energy $E_{\rm P}$ integrated over the 3D computation box,

$$E_{\text{free}} = E_{\text{NP}} - E_{\text{P}} = \int \frac{1}{8\pi} B_{\varphi}(\mathbf{x})^2 \ q_{\text{iso}} \ dV,$$
 (23)

where $q_{\rm iso} = (\pi/2)^2 \approx 2.5$ is a correction factor that generalizes the vertical twist orientation to isotropy (Aschwanden et al. 2014b).

The main task of our VCA-NLFFF code is then to optimize the non-potential-field parameters α_m , $m=1,\ldots,n_{\rm mag}$ by forward-fitting to observed loop coordinates [x(s),y(s)], which is accomplished by minimizing the misalignment angles $\mu_{i,j}$ between the theoretical magnetic field model $\mathbf{B}^{\rm theo} = \mathbf{B}^{\rm np}$ and the observed loop directions $\mathbf{B}^{\rm obs}$,

$$\mu_3 = \cos^{-1} \left(\frac{(\boldsymbol{B}^{\text{theo}} \cdot \boldsymbol{B}^{\text{obs}})}{|\boldsymbol{B}^{\text{theo}}| \cdot |\boldsymbol{B}^{\text{obs}}|} \right), \tag{24}$$

where the 3D misalignment angles $\mu_{i,j}$ are measured for $i=1,...,n_{\rm loop}$ loops at a number of $j=1,...,n_{\rm seg}$ segments along each loop. The optimization criterion minimizes the median of all $\mu_{i,j}$ values.

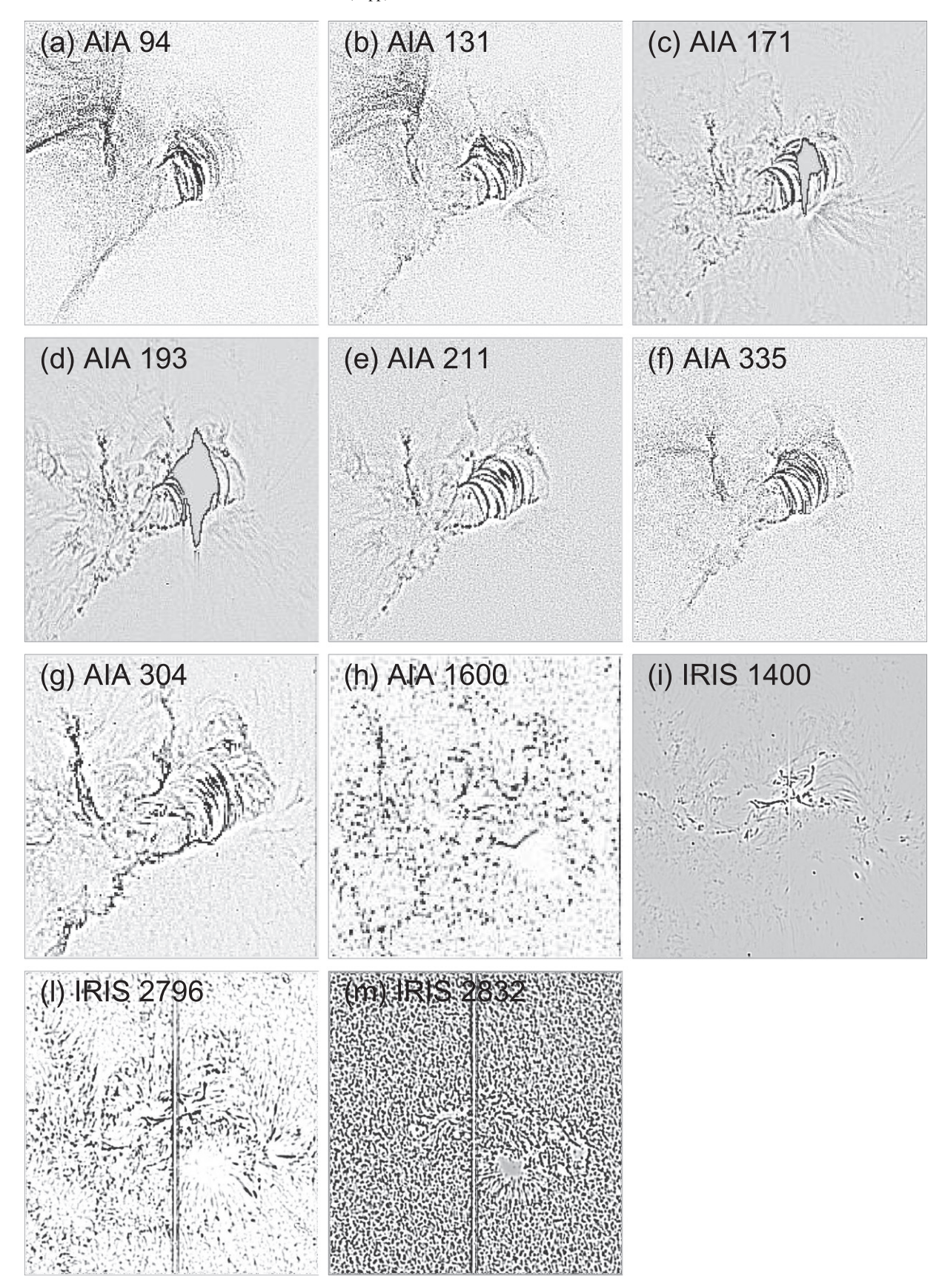


Figure 9. Example of highpass-filtered images, observed on 2014 March 29, 18:17 UT with AIA, and at 17:35 UT with *IRIS*. The images were obtained with a lowpass filter of $n_{\text{sm1}} = 1$ and a highpass filter of $n_{\text{sm2}} = 3$. Otherwise, respresentation is similar to Figure 3.

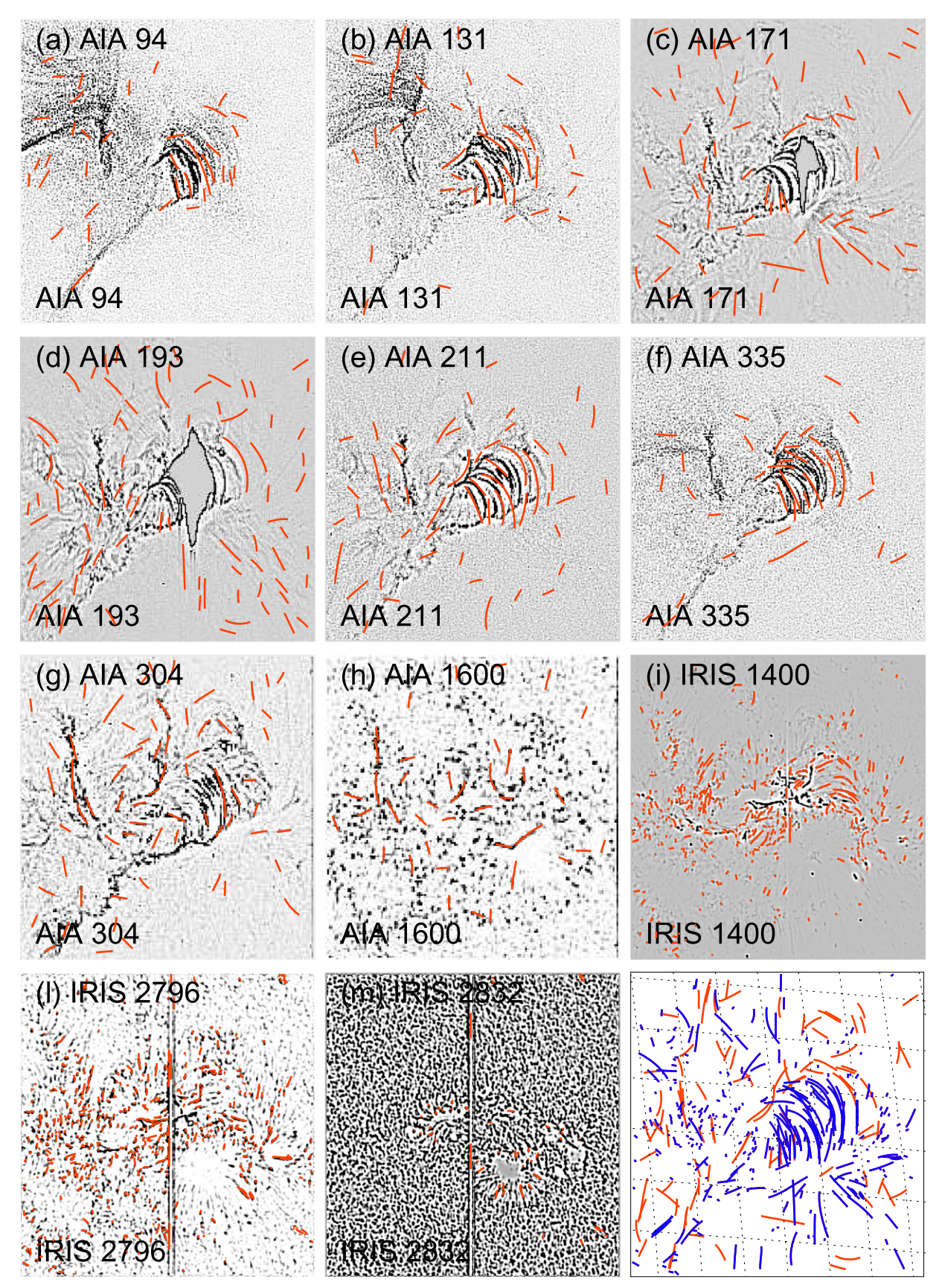


Figure 10. Example of automated tracing of curvi-linear features, applied to the highpass-filtered images shown in Figure 9, observed on 2014 March 29, 18:17 UT with AIA, and at 17:35 UT with IRIS. The combination of the tracings in all wavelengths is shown in the bottom right panel. All detected structures are marked with red, while the fitted structures (with a misalignment of $\leq 20^{\circ}$) are marked with blue. Otherwise, the respresentation is similar to Figures 3 and 9.

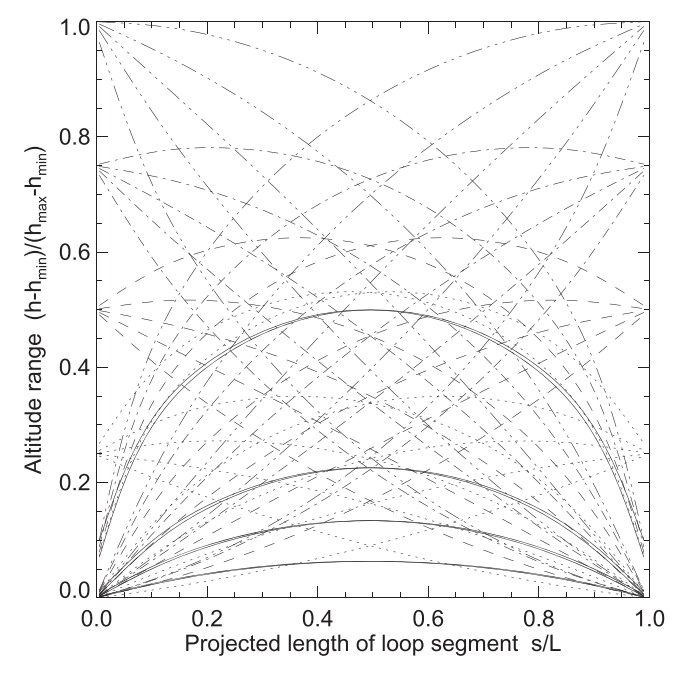


Figure 11. Modeling of the altitude coordinate h(s) of loop segments observed in 2D, using a selected subset of circular geometries in the loop plane. The loop segments are all circular, but have different altitudes for the footpoints and apices, and different angular ranges of a semi circle. The loop segments are shown here with a normalized projected length s/L (x-axis) and a normalized height range $(h - h_{\min})/(h_{\max} - h_{\min})$ (y-axis).

5.2. Numerical Code

The numerical implementation of the VCA-NLFFF code has been gradually improved over time, including significant changes that are different from earlier numeric code versions (Aschwanden & Sandman 2010; Sandman & Aschwanden 2011; Aschwanden et al. 2012, 2014a, 2014b; Aschwanden 2013b, 2013c, 2015; Aschwanden & Malanushenko 2013).

The VCA-NLFFF code starts with the parameters of the magnetic charges that were obtained from the potential field fit to the line-of-sight magnetogram and adds an additional forcefree α -parameter for each magnetic charge, so that we have a parameterization of $(x_m, y_m, z_m, B_m, \alpha_m)$, for $m = 1, ..., n_{\text{mag}}$. On the other side, we have the input of loop coordinates $[x_{ij}, y_{ij}]$ from $i = 1,...,n_{loop}$ loops measured at $j = 1,...,n_{seg}$ segments, where n_{seg} is interpolated to a fixed number of $n_{\text{seg}} = 9$ segments, regardless how long the loops are, so that each loop or loop segment has the same weight in the fitting. Of course, the third coordinates z_{ij} , the line-of-sight coordinates of each loop are not known a priori, but lower and upper boundaries are given by the photospheric height $h_{\min} = 0$ and by the upper boundary of the computation box at a chosen height of $h_{\rm max}=0.2$ solar radii. In the recent versions of the code, an approximate geometry of the height dependence is fitted to each loop segment. This approximate geometry encompasses a circular segment that extends over an arbitrary height range $0 < [h_1, h_2] < h_{\text{max}}$, has a variable orientation of the loop plane, a variable range of curvature radii, and covers a variable angular range of a full circle. The loop segment can appear as a half circle, a concave or convex circular segment, of even as a straight line in the extreme limit. A set of such circular geometries is visualized in Figure 11. Alternative geometries used in the parameterization of the height dependence are Bezier spline functions (Gary et al. 2014). Fitting the 2D projections of this set of variable circular geometries in height to the 2D projections of the observed loop coordinates $[x_{ij}, y_{ij}]$ yields then the best-fit line-of-sight coordinates z_{ij} for each loop segment, as well as the vector components of the loop directions at each location (i,j),

$$\mathbf{v}_{ij} = [(x_{i,j+1} - x_{i,j-1}), (y_{i,j+1} - y_{i,j-1}), (x_{i,j+1} - z_{i,j-1})].$$
(25)

The code calculates then the misalignment angle μ_2 in 2D (in the x–y-plane) and the 3D misalignment angle μ_3 from the scalar product (Equation (24)) between the observed loop direction v_{ij} and the magnetic field vector $\boldsymbol{B}_{ij}^{\rm np}$, or the potential field (Equation (11)), of a trial non-potential magnetic field (Equations (17), (18), (22)) based on the set of variables α_m , $m = 1, ..., n_{\rm mag}$. Thus, in this first iteration step of the forward-fitting procedure we obtain a set of 3D misalignment angles $\mu_{3,ij}$ for each loop segment, from which we define an optimization parameter by taking the median of all misalignment angles,

$$\mu_3 = \text{median}(\mu_{3ii}), i = 1, ..., n_{\text{loop}}, j = 1, ..., n_{\text{seg}}.$$
 (26)

In the second half of an iteration procedure we optimize the global misalignment angle μ_3 with the minimization procedure of Powell's method in multi-dimension (Press et al. 1986, p. 294), which calculates in each iteration cycle all gradients $(\partial \mu/\partial \alpha_m)$, $m=1,...,n_{\rm mag}$ of each magnetic charge parameter α_m , and improves the next iteration value by

$$\alpha_m^{\text{new}} = \alpha_m^{\text{old}} - \Delta \alpha_0 \frac{(\partial \mu / \partial \alpha_m)}{\max[(\partial \mu / \partial \alpha_m)]}, \tag{27}$$

which optimizes the misalignment angles by

$$\mu^{\text{new}} = \mu^{\text{old}} + \Delta \alpha_0 (\partial \mu / \partial \alpha_m), \tag{28}$$

where $\Delta\alpha_0=1.0~R_\odot^{-1}$ is the maximum increment of change in α_m during each iteration step. After the first iteration cycle is completed, a second (or subsequent) cycle is performed, in each one first optimizing the altitudes to obtain an improved third coordinate z_{ij} , and then optimizing the α_m . The final result of a NLFFF solution is contained in a set of coefficients $(x_m, y_m, z_m, B_m, \alpha_m)$, $m=1,\dots,n_{\rm mag}$, from which a volumefilling NLFFF solution ${\bf B}_{\rm np}=[B_x(x,y,z),B_y(x,y,z),B_z(x,y,z)]$ can be computed in the entire computation box. Individual field lines can be calculated from any starting point (x,y,z) by sequential extrapolation of the local ${\bf B}$ -field vectors in both directions, until the field line hits a boundary of the computation box.

One of the biggest challenges is the elimination of "false" loop tracings, which occur due to insufficient spatial resolution, over-crossing structures, moss structures (Berger et al. 1999; De Pontieu et al. 1999), data noise, and instrumental effects (image edges, vignetting, pixel bleeding, saturation, entrance filter mask, etc.). While we attempted to identify such irregularities in earlier code versions, we find it more efficient to eliminate "false" structures iteratively based on their excessive misalignment angle. In the present code, "false" tracings are automatically eliminated in each iteration step if they exceed an unacceptable large value of the misalignment angle. In the latest version of the code we set a final limit of $\mu_0 \leqslant 20^\circ$ for the 2D misalignment angle, $\mu_2 \leqslant \mu_0$, which is

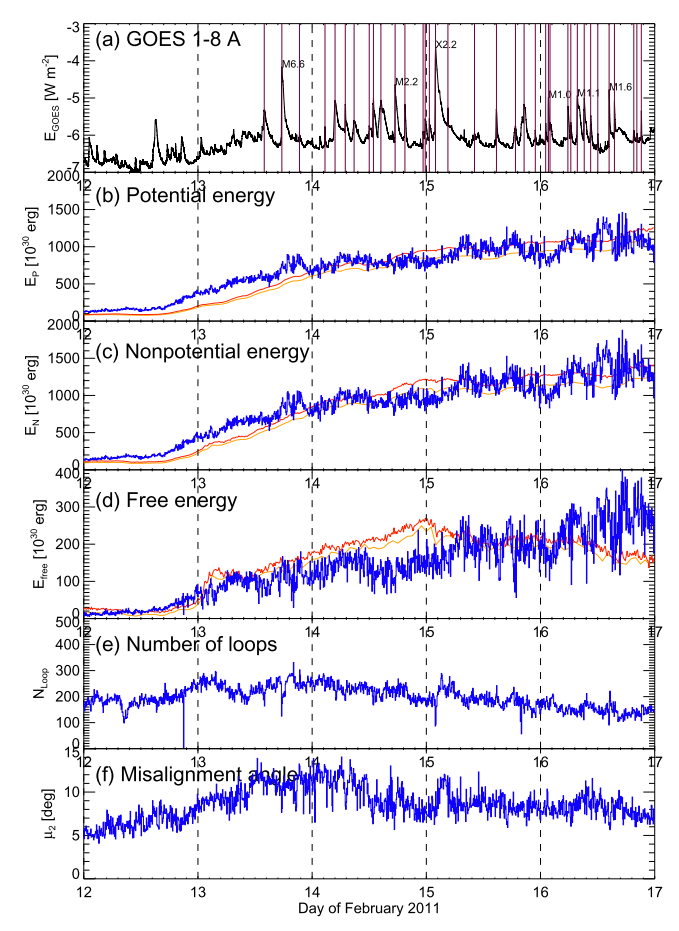


Figure 12. Time evolution of magnetic energies of AR 11158 during 2011 February 12–17: (a) *GOES* 1–8 Å flux, with *GOES* C-, M-, and X-class flares indicated with purple vertical lines. (b) Potential-field energy $E_{\rm P}$. (c) Nonpotential energy $E_{\rm N}$. (d) Free energy $E_{\rm free} = E_{\rm N} - E_{\rm P}$. (e) The number of fitted loops $N_{\rm loop}$. (f) The 2D misalignment angle μ_2 of the best fit. The color code indicates forward-fitting of traced loops with the VCA-NLFFF code in 6 minute time intervals (blue), the W-NLFFF code in 12 minute intervals (red) and 1 hr intervals (orange; Sun et al. 2012a).

gradually approached after a sufficient number of iteration steps to warrant convergence. We set a minimum number of $n_{\rm itmin}=40$ iteration steps, during which the the maximum acceptable misalignment angle limit μ_0 is linearly reduced from $\mu_0=90^\circ$ to the final limit of $\mu_0=20^\circ$. The maximum number of iterations is limited to $n_{\rm itmax}=100$.

5.3. Performance Test: Active Region NOAA 11158

The most extensive data set of potential, non-potential, and free energies, computed with both a traditional NLFFF code and our alternative VCA-NLFFF code is available from NOAA active region 11158, observed during the 5 days of 2011 February 12–17 (Aschwanden et al. 2014a). We already compared the potential energies obtained with both codes in Figure 6. A time-dependent comparison of the energies obtained with both codes is shown in Figure 12. Interestingly, the agreement between the VCA-NLFFF code the W-NLFFF code is quite good (within \lesssim 20%) during all 5 days, for the potential (Figure 12(b)), the non-potential (Figure 12(c)), as well as for the free energy (Figure 12(d)), which represents a large improvement over previous studies (see Figure 8 in Aschwanden et al. 2014a), where the free energy obtained with VCA-NLFFF is substantially lower than the value from

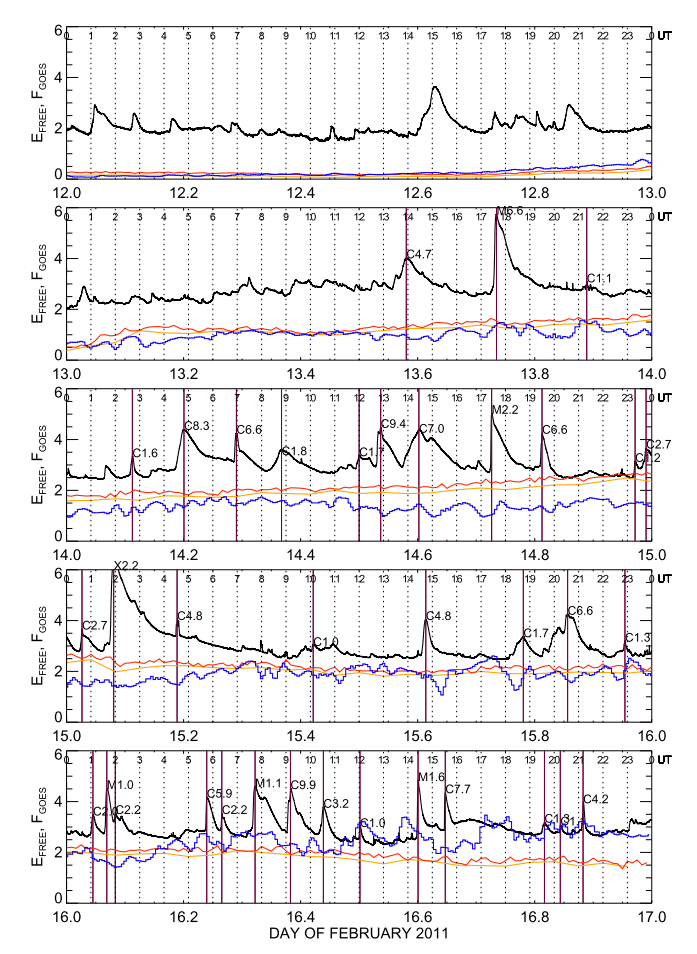


Figure 13. Expanded (three-point median) time profiles of the (logarithmic) *GOES* 1–8 Å flux (black, arbitrary units), the free energies computed with the W-NLFFF code in 12 minute intervals (red) and 1 hr intervals (orange; Sun et al. 2012a), with the VCA-NLFFF code in 6 minute intervals (blue). The times of 36 *GOES* C-, M-, and X-class flares occurring in AR 11158 are indicated with vertical purple lines and labeled with the *GOES* class. Each panel represents a consecutive day from 2011 February 12 to 17.

W-NLFFF during all days (June 13–17) except for the first day when the energies have the lowest values. The good agreement indicates a higher degree of fidelity for both the VCA-NLFFF and the W-NLFFF code, at least in the temporal average. The short-term fluctuations are much larger when modeled with the VCA-NLFFF code, and at this point we cannot discern whether the VCA-NLFFF code produces a larger number of random errors, or whether the W-NLFFF code produces too much temporal smoothing due to the preprocessing procedure.

In Figure 13 we show the expanded time profile plot that corresponds to Figure 9 in Aschwanden et al. 2014a). The displayed time profile of the free energy $E_{\rm free}(t)$ (blue curve in Figure 13) represents the three-point median values (smoothed with a boxcar of three pixels), which eliminates single-bin spikes (with a cadence of 6 minutes here). The time profile $E_{\rm free}(t)$ exhibits many fewer random fluctuations than the previous results (Figure 10 in Aschwanden et al. 2014a), which indicates that the remaining fluctuations are more likely to be real changes in the free energy. Indeed, most of the *GOES* flares show a corresponding dip or decrease in the free energy, although the detailed timing is not always strictly simultaneous. In contrast, the time profile of the free energy $E_{\rm free}(t)$

determined with W-NLFFF shows almost no temporal fluctuations, and only very small changes or decreases after a flare, if at all. We suspect that the preprocessing procedure of the W-NLFFF code over-smoothes changes in the free energy, and thus underestimates the dissipated energy in a flare. It was already previously noticed that the W-NLFFF code yields about an order of magnitude lower energy decreases during flares than the VCA-NLFFF code (see Figure 11 in Aschwanden et al. 2014a).

During the observing time interval of 2011 February 12–17, a total of 36 GOES C, M, and X-class flares were identified in the NOAA flare catalog. For most of these 36 events we see a significant decrease of free energy with the VCA-NLFFF method. We show nine examples with the most significant energy decreases in Figure 14, for both the VCA-NLFFF and the W-NLFFF method. We show the slightly smoothed (threepoint median) evolutionary curves, from which the energy decrease $\Delta E_{\text{free}} = E_{\text{free}}(t_2) - E_{\text{free}}(t_1)$ is measured between the maximum energy before, and the minimum energy after the flare peak time, allowing for a time margin of ± 0.5 hr, i.e., $t_{\text{start}} - 0.5 < t_1 < t_{\text{peak}}$ and $t_{\text{peak}} < t_2 < t_{\text{end}} + 0.5$. The free energy $E_{\text{free}}(t)$ agrees well between the VCA-NLFFF and the W-NLFFF code, as mentioned before (Figure 12(d)), but the energy decreases during flares are much more pronounced with the VCA-NLFFF code than with the W-NLFFF code, which may indicate that the W-NLFFF code suffers from oversmoothing in the preprocessing procedure.

In Figure 15 we compile the decreases of the free energy $-\Delta E_{\rm free}$ during flares as a function of the free energy $E_{\rm free}$ before the flare and find that in the average 21% of the free energy is dissipated during flares according to the VCA-NLFFF code, or 11% according to the W-NLFFF code. This is similar to the earlier study (Figure 11 in Aschwanden et al. 2014a). Thus there is a discrepancy of a factor of \approx 2 between the VCA-NLFFF and the W-NLFFF code.

5.4. Performance Test: X-class Flares

In Figures 16 and 17, we present the results of the free energy evolution $E_{\text{free}}(t)$ for 11 X-class flare events, which includes all X-class events that occurred in the first three years of the SDO mission (Aschwanden et al. 2014b). For each flare we show the GOES light curve, the GOES time derivative (which is a proxy for the hard X-ray emission according to the Neupert effect), and the evolution of the free energy according to both the VCA-NLFFF and the W-NLFFF codes. Since the X-class flares are the most energetic events, we expect that they exhibit most clearly a step function from a high pre-flare value of the free energy to a lower post-flare level after the flare. Such a step function is most clearly seen with the W-NLFFF code for flare events #12, #66, #67, and #147 (red diamonds in Figures 16 and 17), and with the VCA-NLFFF code for the events #67 and #384 (blue curve in Figures 16 and 17). The flare event #67 exhibits the best agreement between the W-NLFFF and VCA-NLFFF codes, displaying not only a large step function, but also good agreement between the levels of free energy before and after the flare. No significant energy decrease during the flare time interval is detected for event #148 with the W-NLFFF code, or for event #147 with the VCA-NLFFF code. Generally, the VCA-NLFFF code reveals a larger step of free energy decrease than the W-NLFFF code (Figure 15). Thus we can conclude from the performance tests of the VCA-NLFFF code: (1) a significant decrease in the free energy during X-class flares is detected in 10 out of the 11 cases; (2) the maximum of the energy decrease of free energy occurs within the impulsive flare phase (when hard X-rays or the GOES time derivative culminate), and (3) the energy decreases detected with the VCA-NLFFF code are a factor of \approx 2 larger than detected with the W-NLFFF code.

In Figures 18 and 19 we show the results of the VCA-NLFFF solution for the flare events #67 (X1.8 flare on 2011 September 7), #384 (X1.2 flare on 2014 January 7), and #592 (X1.9 flare on 2014 March 29). We show two representations of the magnetic field solution, one by selecting field lines that intersect with the midpoints of the automatically traced loops (Figure 18), and the other one by a regular grid of field lines with footpoint magnetic field strengths of $B > 100 \,\mathrm{G}$ (Figure 19). Since these events show the most consistent evolution of the free energy decrease with both the VCA-NLFFF and the W-NLFFF code, they should convey most clearly the topology change from a helically twisted nonpotential field before the flare to a relaxed near-potential field after the flare. Figures 18(a) or (b) shows the NLFFF solution at 22:02 UT, just when the free energy reaches the highest value $(E_{\rm free} = 165 \times 10^{30} \, {\rm erg})$ at the start of the flare, which indeed reveals a highly twisted field around the leading sunspot. Figure 18(b) shows the NLFFF solution at 23:08 UT, just after the impulsive flare phase when the free energy drops to the lowest value ($E_{\text{free}} = 14 \times 10^{30} \, \text{erg}$), which indeed exhibits an untwisted, open field above the sunspot, while a post-flare arcade grows in the eastern part of the sunspot, where obviously most of the magnetic reconnection process during the flare took place. The open-field configuration above the sunspot is a consequence of an erupting CME. This example shows an unambiguous magnetic energy decrease by $\approx 90\%$ of the free energy ($\Delta E_{\text{free}} = -151 \times 10^{30} \, \text{erg}$), which is dissipated during a magnetic reconnection process and launch of a CME.

Also the second case shown in Figures 18 and 19 (flare #384, X1.2 class, 2014 January 7), exhibits an untwisting of the magnetic field above the sunspot during the flare, most clearly seen as helical twist in clock-wise direction (Figure 19(c)) that de-rotates clock-wise to an almost radial potential field after the flare (Figure 19(d)). The detection of loop structures appears to be spotty in Figures 18(c) and (d), but the model picks up sufficient field directions around the leading sunspot to measure the untwisting of the sunspot field and the associated magnetic energy decrease.

5.5. Performance Test: AIA versus IRIS

The first X-class flare observed with *IRIS* occurred on 2014 March 29, 17:40 UT, which has already been modeled with a previous version of the VCA-NLFFF code, showing a similar amount of energy decrease in coronal data from AIA (94, 131, 171, 193, 211, 335 Å), chromospheric data from AIA (304, 1600 Å), and in chromospheric data from *IRIS* (1400, 2796 Å). This result delivered the first evidence that both coronal as well as chromospheric features (loops or fibrils) can be used to constrain a non-potential magnetic field model of an active region or flare (Aschwanden 2015). However, the early version of the VCA-NLFFF code was not very sensitive to the faint coronal and chromospheric features during the pre-flare phase, so that substantially less free energy was detected during the pre-flare phase than is found with the improved VCA-NLFFF code. This lack of coronal and chromospheric structures in the

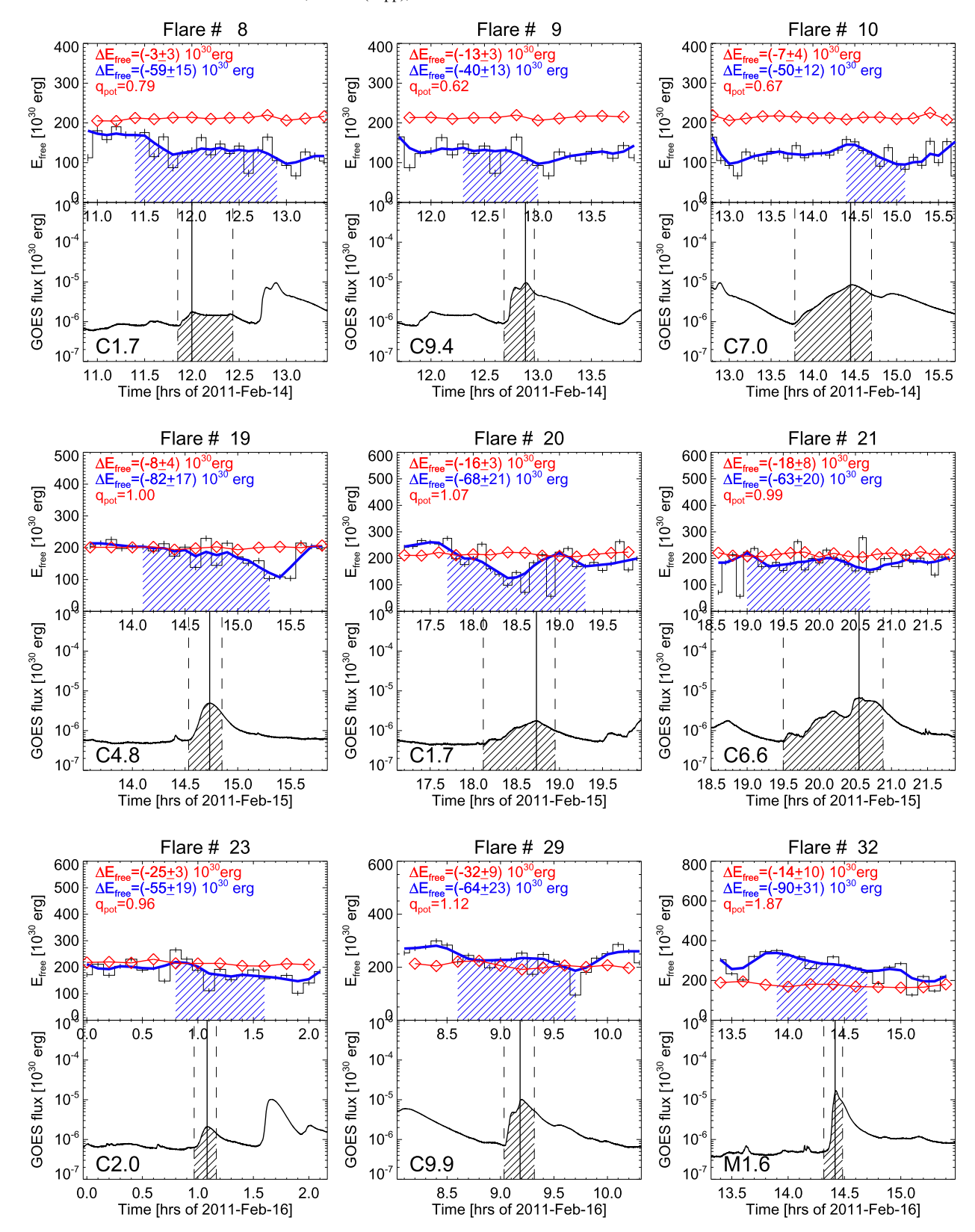


Figure 14. Time evolution of the free energy $E_{\text{free}}(t)$ is shown for nine flare events occurring in AR 11158 during 2011 February 12–17. The nine events were selected by the largest significance of energy decreases ΔE_{free} during the *GOES* flare duration, including a time margin ± 0.5 hr before and after the flare. The free energy is determined with the W-NLFFF code (red diamonds), and independently with the VCA-NLFFF code (histogram with error bars), rendered as three-point median (blue curve). The time interval with energy decrease is marked with a blue hatched area. The *GOES* flux is shown on a logarithmic scale. The time interval between start and end of the flare is marked with a hatched (black) area.

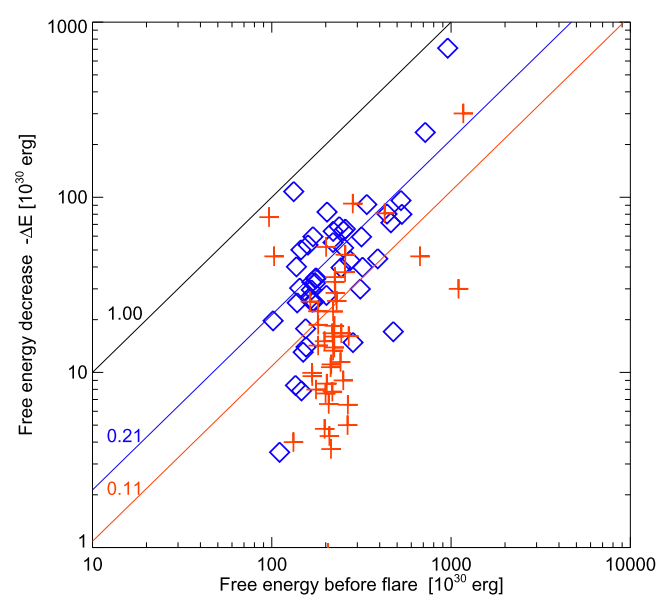


Figure 15. Decreases of the free energy decrease during 36 flares of AR 11158 and 11 X-class flares are plotted versus the free energy before the flare, as measured with the VCA-NLFFF code (blue diamonds) and the W-NLFFF code (red crosses). Note that VCA-NLFFF yields an energy decrease from the preflare free energy by 21% (in the (logarithmic average), while the W-NLFFF code detects about half of this value (11%).

pre-flare phase was interpreted in terms of a coronal illumination effect, conveyed by filling of coronal loops with the chromospheric evaporation process. However, since the new VCA-NLFFF code is sufficiently sensitive to detect non-potential structures in the pre-flare phase, an explanation in terms of a coronal illumination effect is not needed anymore.

In Figures 20 and 21 we show new results of the evolution of the free energy $E_{\text{free}}(t)$ for the 2014 March 29 flare, independently modeled with the VCA-NLFFF code in three different wavelength domains and with two independent instruments (AIA and IRIS). The representation of the results in Figure 20 can be compared with Figure 3 in Aschwanden (2015). We detect about the same free energy at the flare peak, $E_{\rm free}(t_{\rm peak}) \approx 40 \times 10^{30} \, {\rm erg}$ versus $E_{\rm free}(t_{\rm peak}) = (45 \pm$ $2) \times 10^{30}$ erg earlier (Figure 3 in Aschwanden 2015). We find about the same decrease in the free energy, $E_{\rm free}(t_{\rm peak}) \approx 30 \times 10^{30} \, {\rm erg}$ flare peak, $E_{\text{free}}(t_{\text{peak}}) = (29 \pm 3) \times 10^{30} \,\text{erg}$ earlier (Figure 3 in Aschwanden 2015). However, what is much better than in the previous study is the pre-flare level of the free energy, being significantly higher than the post-flare level, which is expected in the simplest scenario of magnetic energy dissipation. Therefore, the present VCA-NLFFF can be considered to be superior compared to earlier (less sensitive) versions. The change in the magnetic configuration during the flare shows an untwisting in counter clock-wise direction (Figures 19(e) and (f)), while the sigmoidal bundle of field lines in the north–east sector of the sunspot (Figure 19(e)) evolves into a near-potential dipolar post-flare loop arcade (see yellow loop tracings in Figure 18(f)).

5.6. Performance Test: Parametric Study

Finally, we perform a parametric study in order to investigate the robustness and sensitivity of the VCA-NLFFF solutions to the control parameters of the numerical code. A list of 24 control parameters is given in Table 1, which includes four groups, one specifying the data selection (instrument, spatial resolution, wavelength, and FOV choice), a second one with four control parameters enables the potential-field deconvolution, a third one with nine control parameters enables the automated loop tracing, and a fourth one with seven control parameters enables the forward-fitting. In order to assess the robustness of the VCA-NLFFF code, we investigate how a variation of the control parameters affects the results of the evolution of the free energy $E_{\text{free}}(t)$ (Figures 21–23). Specifically we show how the time resolution of the data or cadence (Figure 21), the wavelength choice (Figure 22), and the variation of 12 tunable control parameters changes the timedependent free energy values (Figure 23) of the X-flare observed on 2014 March 29 with both AIA and IRIS, of which various data are shown in Figures 3, 4, 9, 10, 18(e), (f), 19(e), (f), and 20.

(1) Cadence: varying the time resolution or cadence from $t_{\text{cad}} = 6 \text{ minutes to } 3, 2, \text{ and } 1 \text{ minutes (Figures 21, 23(a)) we}$ find that the smoothed time profile $E_{\text{free}}(t)$ (using the median values from time intervals that are equivalent to the cadence) are invariant and thus yield exactly the same free energy decreases associated with the flare at any value of the time resolution. This is not trivial, because a factor of 6 times different amount of information that is used between a cadence of 6 and 1 minutes. If the free energies determined with VCA-NLFFF code are entirely due to noise, the energy drop between the pre-flare and post-flare time interval would vary arbitrarily, rather than being invariant. Investigating the evolution of the free energy at a cadence of 1 minute, however, appears to reveal some coherent quasi-periodic fluctuations with an approximate period of $P \approx 3$ minutes (Figure 21 bottom left), which could be associated with the helioseismic global p-mode oscillations (a property that will be examined elsewhere). In Figure 21 we show also the time evolution of the number of detected and fitted loops (Figure 21, middle column), which seems to be roughly constant during this flare and is not correlated with the step-like (dissipative) decrease in free energy. We show also the time evolution of the misalignment angle $\mu_2(t) \approx 10^{\circ}$ (Figure 21, right column), which is essentially constant and is not affected by the flare evolution, although the flare area coverage of automatically traced loops varies substantially during the flare (Figures 18(e) and (f)).

(2) Wavelengths: the choice of wavelengths could crucially affect the accuracy of the inferred free energy, because each wavelength covers only a limited amount of the flare temperature range, and some wavelengths are only sensitive to chromospheric temperatures. In Figure 22 we perform the experiment to determine the evolution of the free energy $E_{\text{free}}(t)$ for each of the 8 AIA and 3 IRIS wavelengths separately. Interestingly, the decrease in the free energy is detected in almost all wavelengths independently, which provides a strong argument for the robustness of the code. The largest energy decrease ($\Delta E_{\rm free} = -(37 \pm 10) \times 10^{30}$ erg is detected in the AIA 211 Å wavelengths, while the smallest amount is found with IRIS 2832 Å, which is a chromospheric line. Combining two wavelengths pair-wise together, we find a consistent energy decrease in each wavelength pair (Figure 23(b)). Consequently, our strategy is to combine all coronal AIA wavelengths (94, 131, 171, 193, 211, 335 Å) as a default, because the joint wavelength response complements hot and cool temperatures in flares and active region areas.

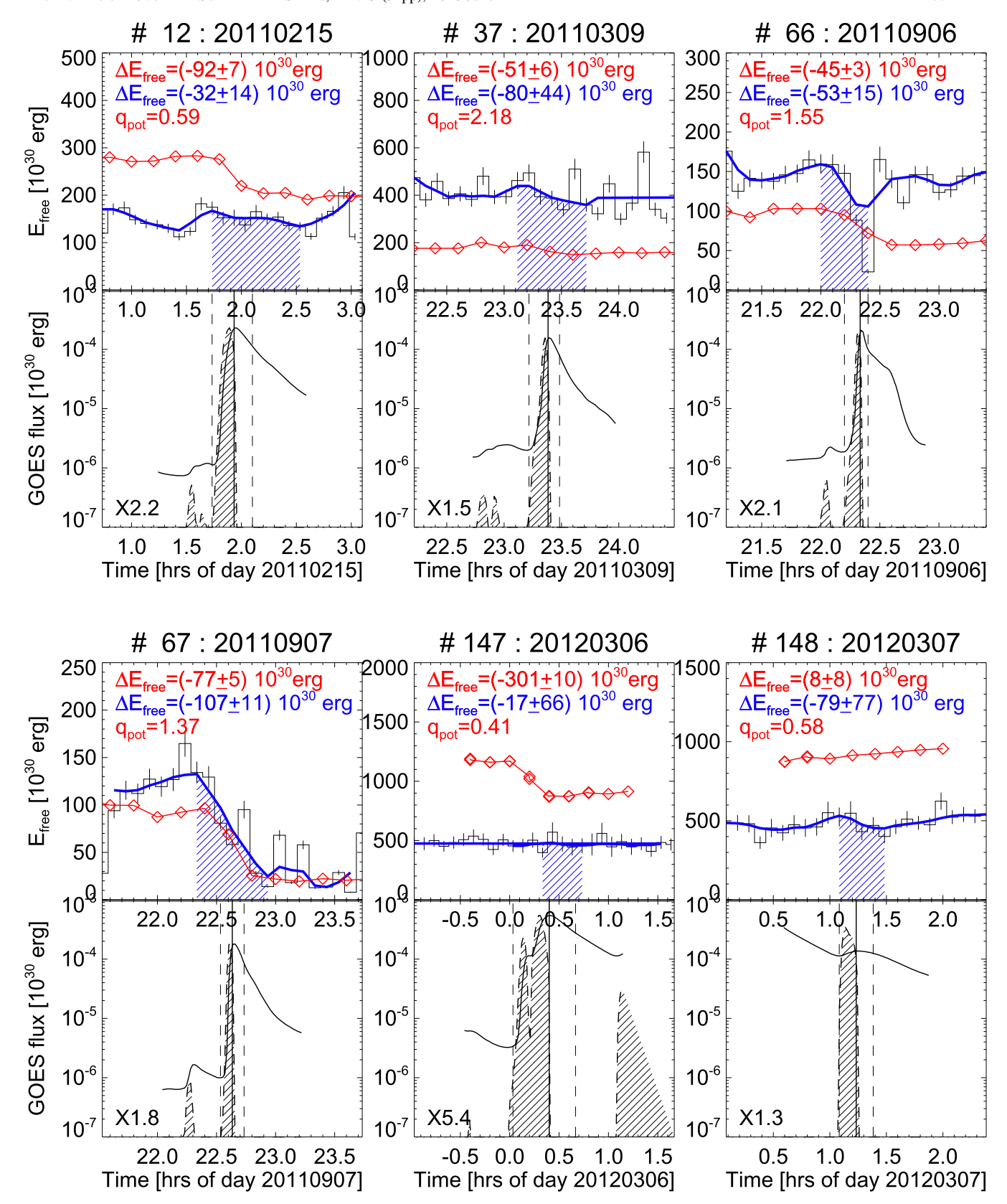


Figure 16. For six X-class flare events we show the evolution of the free energy $E_{\text{free}}(t)$ as determined with the VCA-NLFFF code (blue curve and black histogram) and with the W-NLFFF code (red curve), along with the GOES 1-8 Å light curve. The time interval with decreases in the free energy are marked with a blue hatched area, and the GOES time derivative is marked with a black hatched area.

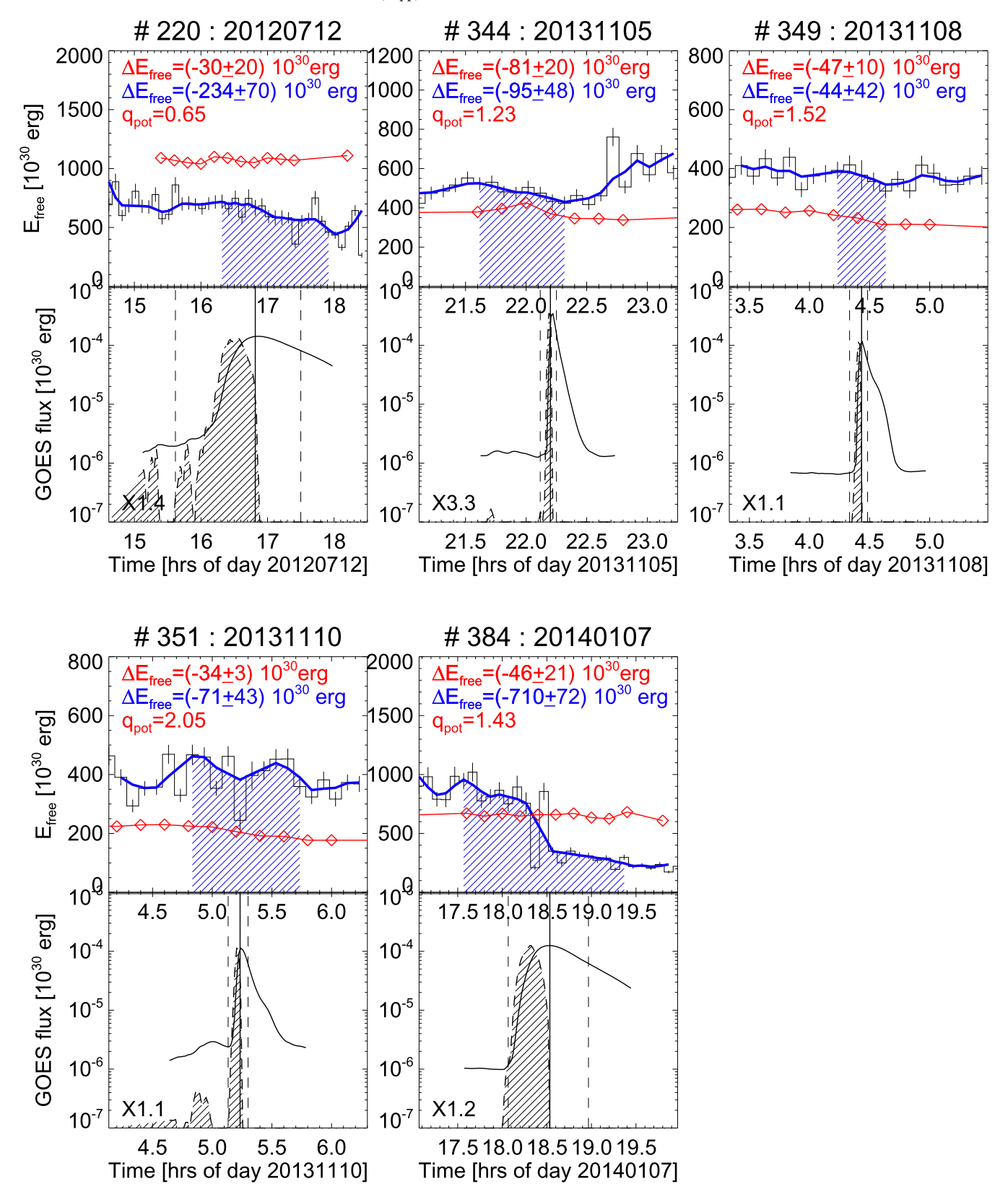


Figure 17. Continuation of Figure 16 with 5 additional X-class flares.

(3) Minimum loop lengths: since the number of loops above some minimum length value $l_{\rm min}$ falls off like a powerlaw distribution function, i.e., $N(>L) \propto L^{-2}$ (Aschwanden et al. 2008), the number of loops that constrain a NLFFF solution

increases drastically toward smaller values on one side, while the ambiguity of true loops and loop-unrelated curved features increases toward smaller values on the other hand. The test shown n Figure 23(c) exemplifies that a value of $l_{\rm min}\approx 4$ or 5

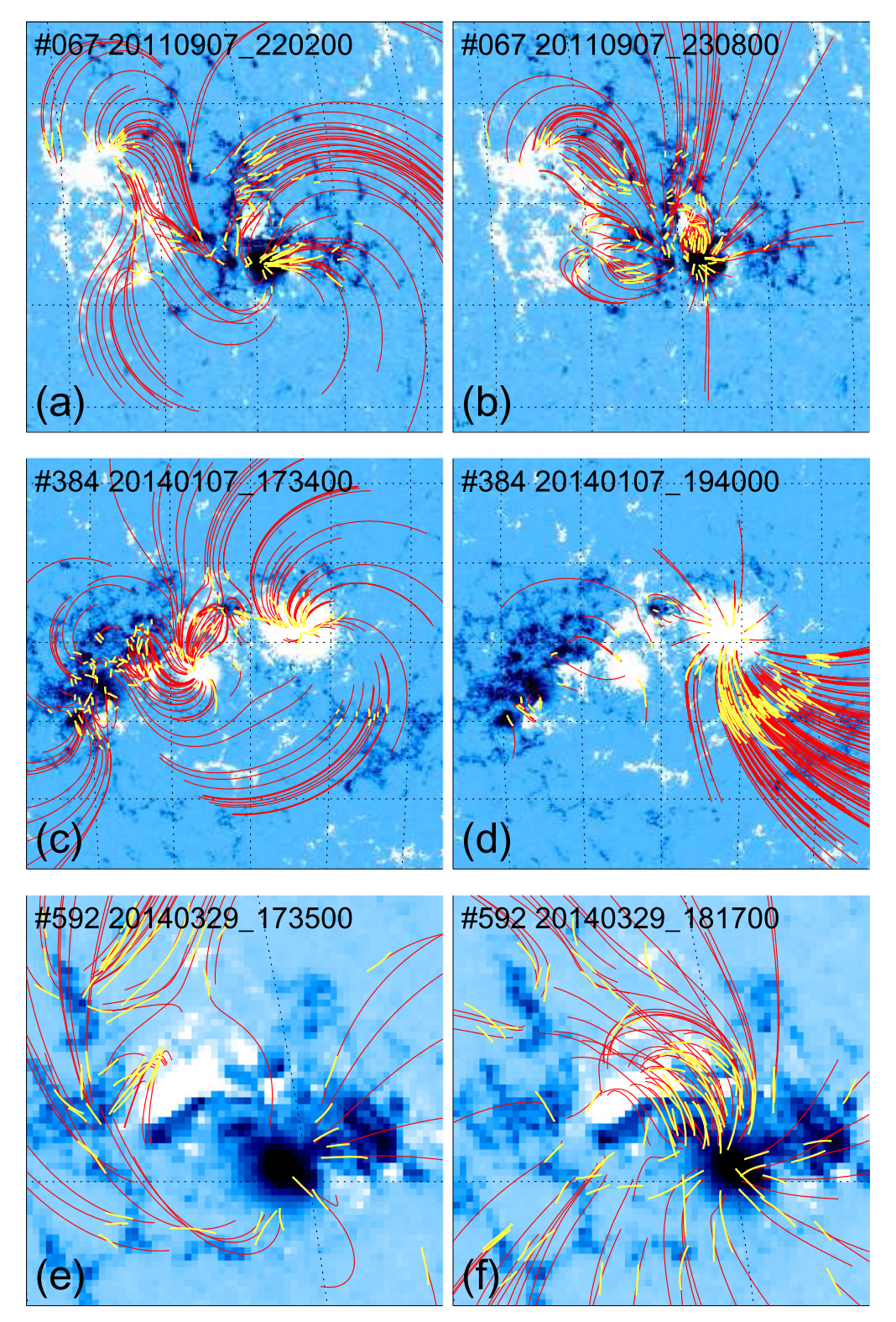


Figure 18. Evolution of the three flares with the most pronounced decrease in free energy are presented at flare start (left panels) and at flare end (right panels). The blue background image represents the B_z HMI magnetogram, the yellow curves present the automatically traced loops, and the red curves represent the best-fit magnetic field based on the VCA-NLFFF code, where only field lines that intersect with the midpoint of the traced loops are shown.

is the optimum, while higher values of $l_{min} = 6$ or 7 lead to slight underestimates of the free energy.

(4) Misalignment angle limit: allowing a large range of 2D misaligned angles $\mu_0 < 45^{\circ}$ clearly hampers the convergence of the VCA-NLFFF code, which implies that data noise

dominates the fit and thus reduces the signal of non-potential-field energies and free energies. The test shown in Figure 23(d) demonstrates that the free energy increases systematically by reducing the misalignment limit from $\mu_0 < 40^\circ$ to $\mu_0 < 10^\circ$. However, if we push the limit to small values, the number of

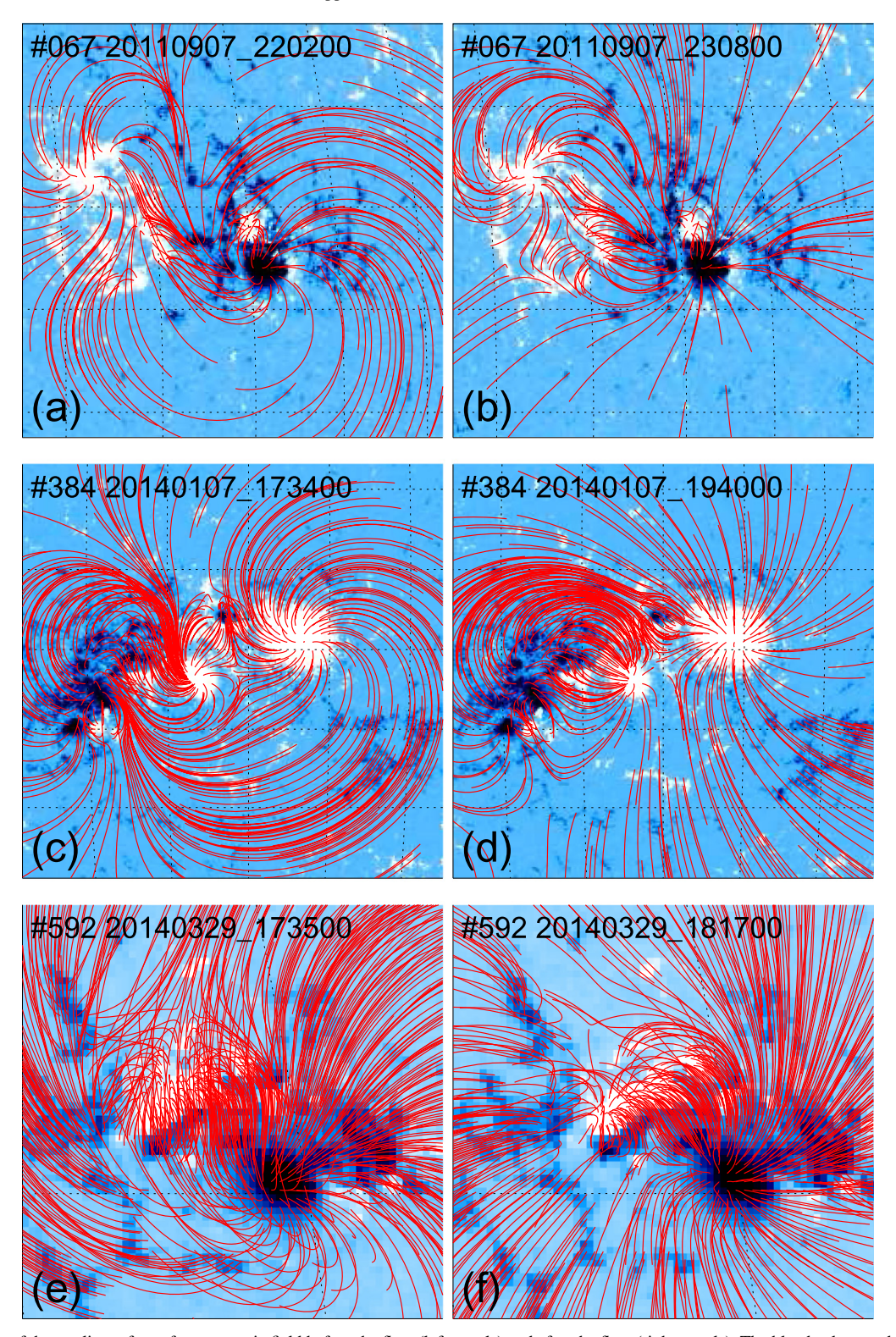


Figure 19. Evolution of the nonlinear force-free magnetic field before the flare (left panels) and after the flare (right panels). The blue background image represents the B_z HMI magnetogram, while the red curves represent the best-fit magnetic field lines computed with the VCA-NLFFF code, selected with footpoints in a 50 \times 50 grid with field strengths of $|B_z| > 100$ G.

fitable features decreases, which has a diminishing effect on the accuracy of a non-potential-field solution. Therefore we choose a compromise of $\mu_0 < 20^\circ$.

(5) Minimum number of iterations: the number of iterations in the forward-fitting algorithm dictates how quickly misaligned features are eliminated, say for an acceptable limit of

 $\mu_0 < 20^\circ$. Reducing the iterations thus changes the observational constraints of fitable loops faster than the code can converge, and thus can inhibit convergence of the code. The test shown in Figure 23(e) clearly demonstrates that the free energy is only fully retrieved for a larger number of iterations, say $n_{\rm nitmin} \gtrsim 40$.

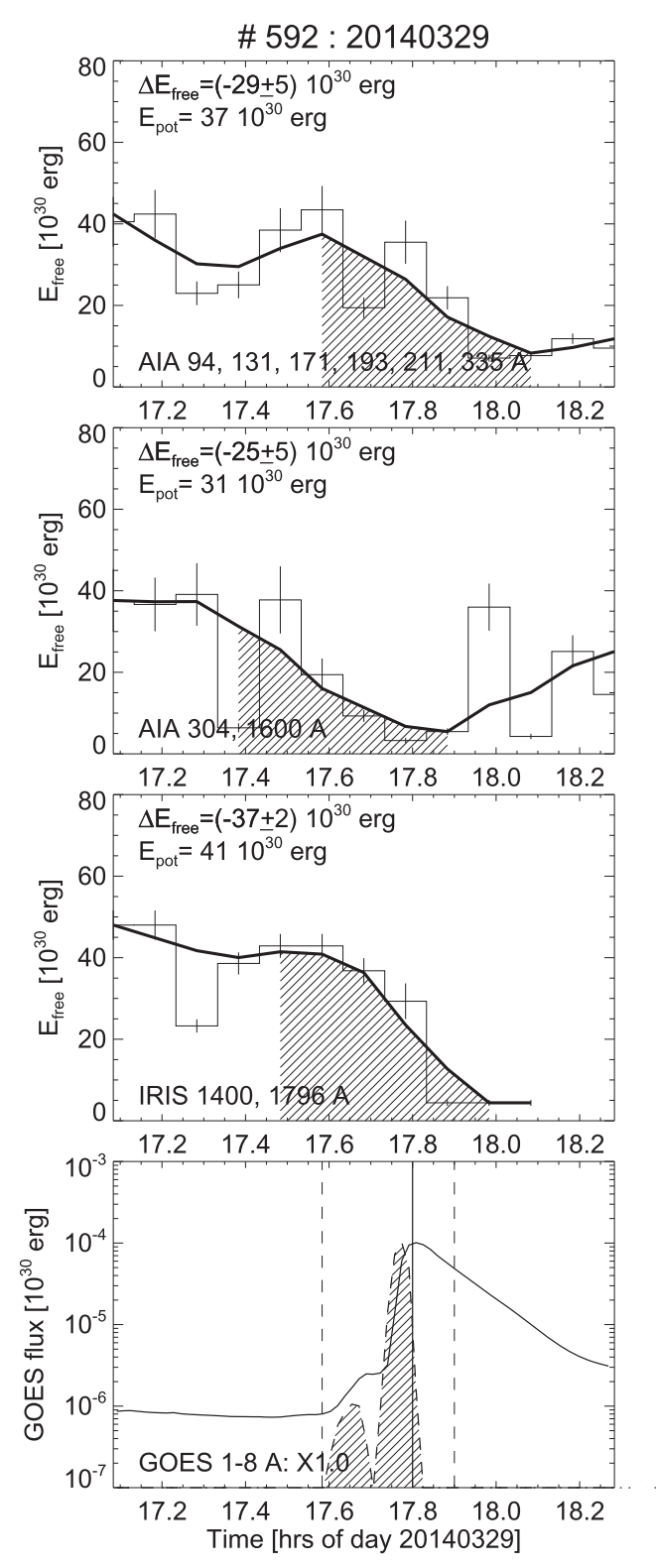


Figure 20. Time evolution of the free energy as measured from AIA in EUV wavelengths (top panel), from AIA UV wavelengths (second panel), from *IRIS* UV wavelengths (third panel), along with the *GOES* 1–8 Å flux (solid linestyle in bottom panel) and *GOES* time derivative (dashed linestyle in bottom panel). The start, peak, and end time of the *GOES* event is indicated with vertical lines.

(6) Spatial smoothing of EUV image: the test shown in Figure 23(f) indicates that smoothing of the EUV loop image with $n_{\rm smo} = 1$, 2, or 3 reduces the estimate of the free energy because faint and thin loop structures are eliminated, which

reduces the observational constraints and accuracy of the forward-fitting code.

- (7) Number of magnetic sources: we expect that increasing the number of magnetic sources increases the accuracy of the free energy. The test shown in Figure 23(g), however, shows the opposite, probably because too many small magnetic sources counter-balance the opposite polarities of closely spaced pairs of magnetic sources, and thus diminishes the total non-potential or free energy. We thus choose a relatively small number of $n_{\rm mag} = 30$ magnetic sources, which also speeds up the computation time of a VCA-NLFFF solution.
- (8) Flux and flux filter thresholds: the tests shown in Figures 23(h) and (i) indicate that the threshold of detecting loop structures is not critical, as long as we detect a sufficient number of structures. We choose therefore the lowest threshold values of $a_1, \dots, a_n = 0$ and $a_n, \dots, a_n = 0$.
- values of $q_{\rm thresh,1}=0$ and $q_{\rm thresh,2}=0$. (9) Magnetic proximity: in a previous version of the VCA-NLFFF code we used a distance limit $d_{\rm prox}$ of a loop position to the next location of a magnetic source to eliminate "false" loop detections. The test shown in Figure 23(1) demonstrates that large distance limits of $d_{\rm prox}=4$ or 10 source depths (which is about equivalent to the apparent full width of a magnetic source at the solar surface) does not effect the accuracy of the free energy estimate, while very short limits of $d_{\rm prox}=1$ or 2 eliminate too many relevant structures and thus leads to underestimates of the free energy.
- (10) Loop curvature radius limit: the lower limit of the curvature radius of automatically detected structures is important to exclude "false" curvi-linear structures that occur through coagulation of random structures. The test in Figure 23(m) with curvature radii limits of $r_{\rm min}=4,6,8,$ and 10 pixels demonstrates an invariant free energy profile, and thus no sensitivity of the free energy to the curvature radius limit.
- (11) FOV: if the FOV is too small, the free energy is retrieved only partially. The test shown in Figure 23(n) indicates indeed a steady increase of the free energy from FOV = 0.08 to 0.14 solar radii. On the other side, an upper limit of the FOV is given by the distance to the next neighbored active region.

In summary, our parametric tests are performed on 12 parameters, each one with four variations, for a time profile of the free energy with 13 time steps, yielding a total of 624 VCA-NLFFF solutions. The test results shown in Figure 23 show us at one glance that all of the 48 time profiles exhibit clearly the step-wise decrease of the free energy during a flare, corroborating the robustness of our VCA-NLFFF code. Even the magnitude of the energy decrease agrees within $\approx 20\%$ for each parameter combination.

An estimate of the uncertainty in the determination of the free energy can be made by the number of loops n_{loop} that constrain a solution, which is expected to be according to Poisson statistics,

$$\sigma_{E,\text{free}} = \frac{E_{\text{free}}}{\sqrt{n_{\text{loop}}}}.$$
 (29)

In other words, if only one single loop is used in fitting the VCA-NLFFF magnetic field model, we have an error of 100%, while the error drops down to \lesssim 10% for $n_{\rm loop} \approx$ 100–200, which is a typical value (Figure 21, middle column). However, this error estimate is a lower limit, applicable to the ideal case when a sufficient number of loops is available in the locations

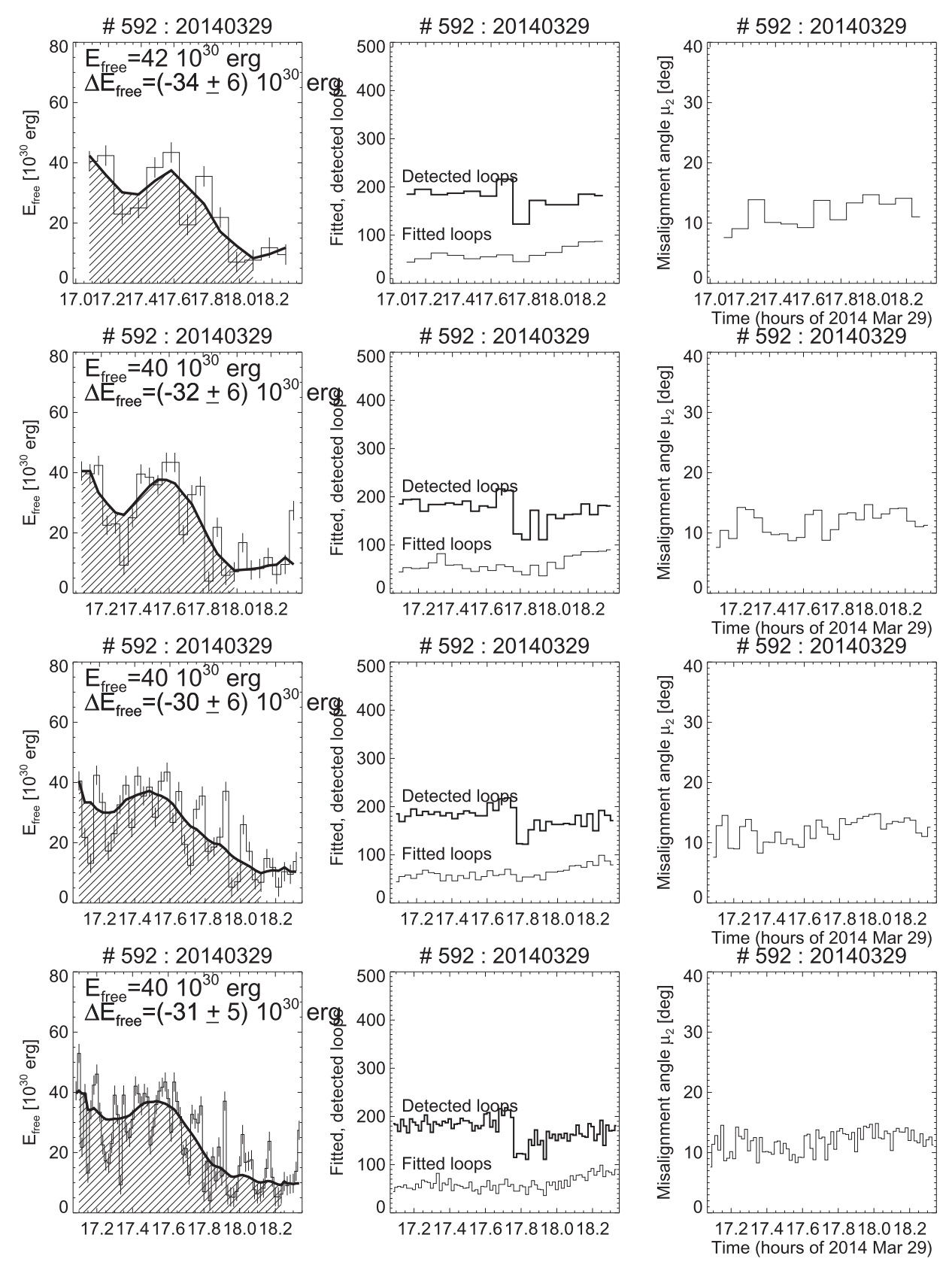


Figure 21. Parametric study of the temporal evolution of the free energy $E_{\text{free}}(t)$ (left column), the number of detected and fitted loop segments (middle column), and the best-fit misalignment angle $\mu_2(t)$ (right column), as a function of different time resolutions: $t_{\text{cadence}} = 6$ minutes (top), $t_{\text{cadence}} = 2$ minutes (second row), $t_{\text{cadence}} = 3$ minutes (third row), and $t_{\text{cadence}} = 1$ minutes (bottom row). Note that the smoothed (three-point median) time profile is invariant to the time resolution of the data.

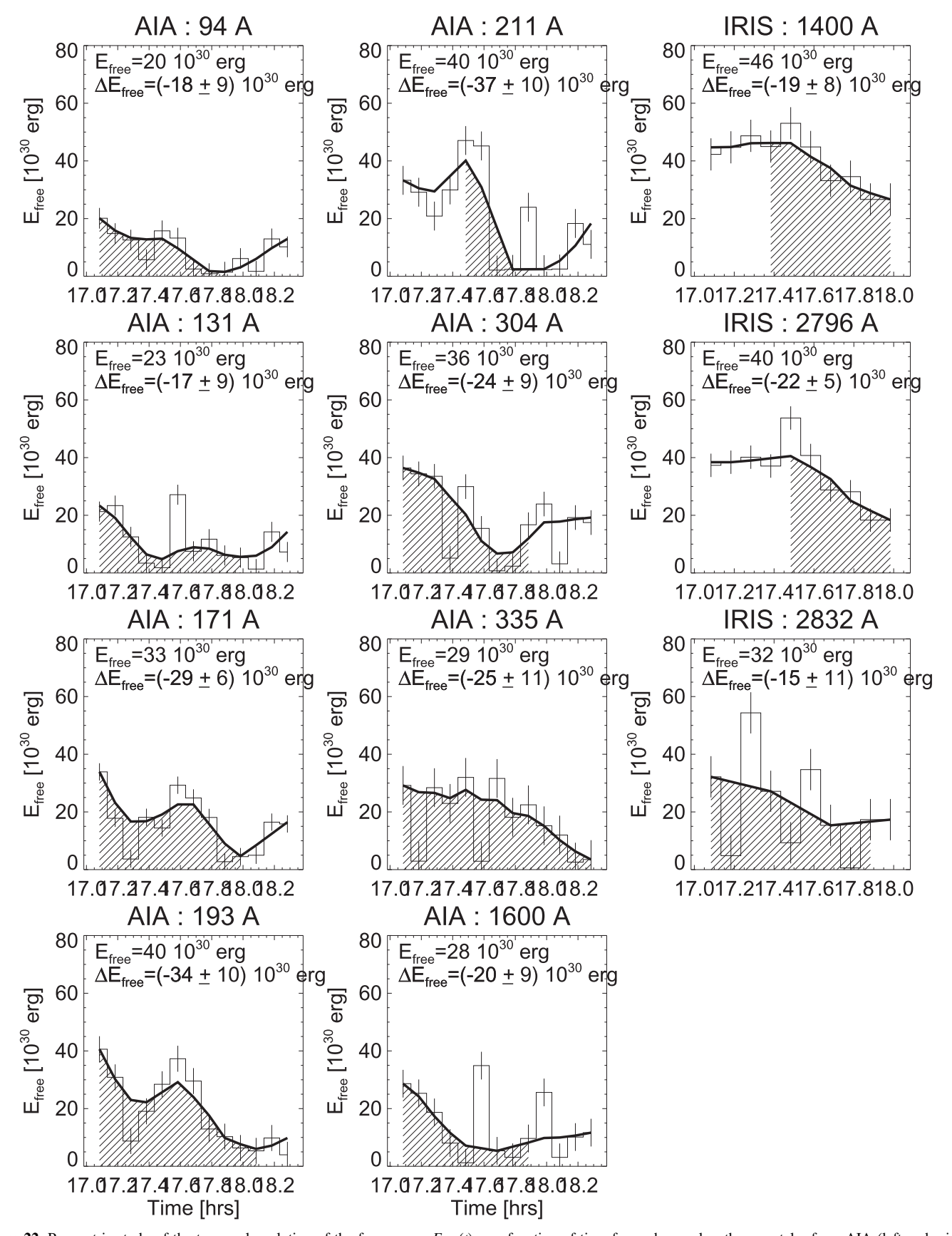


Figure 22. Parametric study of the temporal evolution of the free energy $E_{\text{free}}(t)$ as a function of time for each wavelength separately, from AIA (left and middle column) and IRIS (right column).

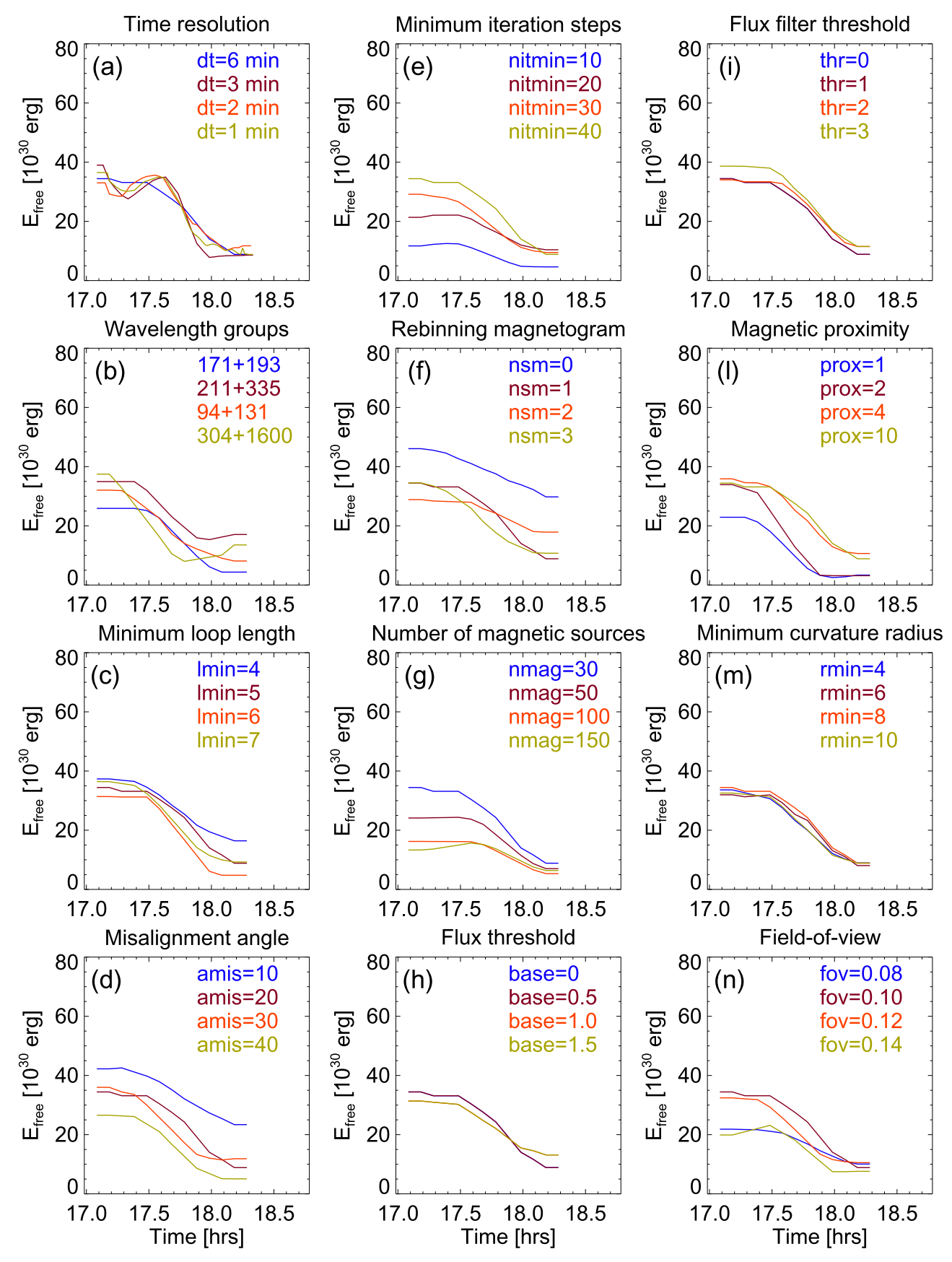


Figure 23. Parametric study of the temporal evolution of the free energy $E_{\text{free}}(t)$ as a function of energy, varying each of the 12 control parameters of the VCA-NLFFF code. Each panel shows the time profile $E_{\text{free}}(t)$ for 4 different values of each control parameter.

of strong magnetic fields. If there is an avoidance of loops near sunspots, no significant amount of free energy is detected, leading to a much larger systematic error than the statistical error due to Poisson statistics of the number of loops.

6. DISCUSSION

The main purpose of the VCA-NLFFF code is the measurement of the coronal magnetic field and its time evolution in active regions and during flares, based on our vertical-current approximation model. The following discussion mostly focuses on the example of active region NOAA 11158 and its famous X2.2 flare in the context of previous studies.

6.1. Magnetic Field Changes in Active Region NOAA 11158

A most studied example is the evolution of active region NOAA 11158, which is the subject of a number of recent papers, focusing on the magnetic evolution of this active region (Jing et al. 2012; Liu & Schuck 2012; Petrie 2012; Sun et al. 2012a, 2012b, 2015; Vemareddy et al. 2012a, 2012b, 2013, 2015; Chintzoglou & Zhang 2013; Dalmasse et al. 2013; Inoue et al. 2013, 2014; Jiang & Feng 2013; Liu et al. 2013; Song et al. 2013; Tarr et al. 2013; Tziotziou et al. 2013; Aschwanden et al. 2014a; Gary et al. 2014; Toriumi et al. 2014; Zhang et al. 2014; Zhao et al. 2014; Guerra et al. 2015; Jain et al. 2015; Kazachenko et al. 2015; Li & Liu 2015; Sorriso-Valvo et al. 2015), or specifically on the X2.2 flare that occurred on 2011 February 15 in this active region (Schrijver et al. 2011; Alvarado-Gomez et al. 2012; Beauregard et al. 2012; Gosain 2012; Jiang et al. 2012; Maurya et al. 2012; Wang et al. 2012, 2013, 2014; Aschwanden et al. 2013a; Petrie 2013; Shen et al. 2013; Young et al. 2013; Malanushenko et al. 2014; Raja et al. 2014; Inoue et al. 2015; Jing et al. 2015), or on the M6.6 flare that occurred on 2011 February 13 in the same active region (Liu et al. 2012; 2013a; Toriumi et al. 2013).

Comparing the workings of the VCA-NLFFF code with the theoretical concepts and observational results that have been published on AR 11158, we have to be aware that the verticalcurrent approximation used in the VCA-NLFFF code implies a slow helical twisting of the sunspot-dominated magnetic field during the energy storage phase, and sporadic episodes of reconnection-driven untwisting during flare times. Therefore, this concept is equivalent to the concept of sunspot rotation (Jiang et al. 2012; Vemareddy et al. 2012a, 2012b, 2013, 2015; Li & Liu 2015). Sunspot rotation forms sigmoid structures naturally, as it is observed in AR 11158 (Schrijver et al. 2011; Jiang et al. 2012; Sun et al. 2012a; Jiang & Feng 2013; Young et al. 2013; Aschwanden et al. 2014a). Strongly twisted magnetic field lines ranging from half-turn to one-turn twists were found to build up just before the M6.6 and X2.2 flare and disappear after that, which is believed to be a key process in the production of flares (Inoue et al. 2013; Liu et al. 2013b). The vortex in the source field suggests that the sunspot rotation leads to an increase of the non-potentiality (Song et al. 2013).

In addition, the energy storage in active region 11158 is also supplied by fast flux emergence and strong shearing motion that led to a quadrupolar (δ -type) sunspot complex (Jiang et al. 2012; Liu & Schuck 2012; Sun et al. 2012a, 2012b; Toriumi et al. 2014). Both the upward propagation of the magnetic and current helicities synchronous with magnetic flux emergence contribute to the gradual energy build up for the X2.2 flare (Jing et al. 2012;

Tziotziou et al. 2013). The amount of non-potential-field energies stored in AR 11158 before the X2.2 *GOES*-class flare was calculated to $E_{\rm np}=2.6\times10^{32}\,{\rm erg}$ (Sun et al. 2012a), $E_{\rm np}=5.6\times10^{32}\,{\rm erg}$ (Tarr et al. 2013), $E_{\rm np}=1.0\times10^{32}\,{\rm erg}$ (COR-NLFFF; Aschwanden et al. 2014a), $E_{\rm np}=2.6\times10^{32}\,{\rm erg}$ (W-NLFFF; Aschwanden et al. 2014a), $E_{\rm np}=10.6\times10^{32}\,{\rm erg}$ (Kazachenko et al. 2015), $E_{\rm np}=2.8\times10^{32}\,{\rm erg}$ (W-NLFFF: Figure 16), $E_{\rm np}=1.8\times10^{32}\,{\rm erg}$ (VCA-NLFFF: Figure 16), which vary within an order of magnitude. The amount of dissipated energy during the X2.2 flare was calculated to $\Delta E_{\rm free}=-1.7\times10^{32}\,{\rm erg}$ (Tarr et al. 2013), $\Delta E_{\rm free}=-1.0\times10^{32}\,{\rm erg}$ (Malanushenko et al. 2014), $\Delta E_{\rm free}=-0.3\times10^{32}\,{\rm erg}$ (Sun et al. 2015), $\Delta E_{\rm free}=-0.6\times10^{32}\,{\rm erg}$ (COR-NLFFF; Aschwanden et al. 2014a), $\Delta E_{\rm free}=-0.6\times10^{32}\,{\rm erg}$ (W-NLFFF; Figure 16), $\Delta E_{\rm free}=-0.3\times10^{32}\,{\rm erg}$ (W-NLFFF: Figure 16), which agree within an factor of \approx 6.

Untwisting of helical fields (as assumed in the VCA-NLFFF model) may not be the full explanation of the magnetic field evolution during flares. Since the VCA concept assumes twisting around vertically oriented axes, untwisting would reduce the azimuthal field component B_{φ} , which corresponds to a reduction of the horizontal field components B_x and B_y (for a location near disk center), as it is the case for the X2.2 flare on 2011 February 15 in NOAA 11158. In contrast, however, the response of the photospheric field to the flare was found to become more horizontal after eruption, as expected from the tether-cutting reconnection model (Liu et al. 2012, 2013b; Wang et al. 2012; Inoue et al. 2014, 2015), or from the *coronal* implosion scenario (Gosain 2012; Wang et al. 2014). On the other side, reduction of magnetic twist was explained by a large, abrupt, downward vertical Lorentz-force change (Petrie 2012, 2013).

In summary, twisting and untwisting of magnetic field lines, the basic concept of our vertical-current approximation model in describing the magnetic evolution, plays a leading role in many of the theoretical and observationally inferred flare models of the X2.2 flare in active region NOAA 11158, and thus justifies the application of the VCA-NLFFF code to flares in general, although the underlying analytical formulation encapsulates only on particular family of solutions among all possible NLFFF solutions.

6.2. The Pros and Cons of NLFFF Codes

After we performed non-potential magnetic field modeling with chromospheric and coronal data we can assess the feasibility of NLFFF modeling in a new light, which we contrast here between the W-NLFFF code and our VCA-NLFFF code. Standard W-NLFFF codes have the following features: (1) they use photospheric vector magnetograph data (where the transverse field components have a much larger degree of noise than the line-of-sight component), (2) they use the assumption of a force-free photosphere, (3) they have no mechanism to fit the magnetic field solution to observed chromospheric or coronal features, (4) they use a preprocessing method to make the photospheric boundary condition more force-free, (5) they are designed to converge to a divergencefree and force-free solution as accurately as possible, (6) the map the sphericity of the Sun onto a plane-parallel boundary, and (7) they are computationally expensive (with computation times in the order of hours or days). In contrast, the VCA-

NLFFF code can be characterized in the following way: (1) it uses only the line-of-sight magnetic field component and avoids the noisy transverse components; (2) it does not use the assumption of a force-free photosphere; (3) it has the capability to minimize the difference between the theoretical magnetic field model and observed curvi-linear features in coronal and/ or chromospheric images; (4) it does not modify the photospheric boundary condition with a preprocessing method; (5) it fulfills the divergence-free and force-free conditions with second-order accuracy; (6) it takes the sphericity of the Sun fully into account, and (7) it is computationally relatively fast (with computation times in the order of minutes). Comparing these seven characteristics, it appears that the VCA-NLFFF code has a superior design in six out of the seven criteria. The only design where the W-NLFFF code has a superior performance is item (5), since they are designed to optimize divergence-freeness, force-freeness, and constancy of the α parameter along each field line, while the VCA-NLFFF code uses an approximate analytical solution that is accurate to second order in α only. However, the reduced accuracy of the VCA-NLFFF code outweighs the biggest short-coming of the W-NLFFF code, i.e., that it is unable to optimize the match between model and observations. The two types of NLFFF codes are truly complementary and one might use the VCA-NLFFF code as a first initial guess that can quickly be calculated before a more accurate NLFFF solution with the W-NLFFF code is attempted. Perhaps it could provide improved boundary conditions for the W-NLFFF code, exploiting both chromospheric and coronal constraints.

We may ask how the uncertainty of NLFFF solutions depends on the magnetic field strength. Intuitively we would expect that weak-field regions have larger relative uncertainties in the transverse field than strong-field regions, due to the relatively larger random noise. For HMI, variability of the mean field strength in the quiet Sun is as much as 5% of the typical weak-field magnitude, where that excursion appears only in the transverse field (Hoeksema et al. 2014). For W-NLFFF solutions, the magnitude of the changes to the vector magnetogram boundary conditions are associated with the remapped vector magnetogram data, and thus tend to be more significant in weak-field regions than in regions of stronger field (see Table 3 in DeRosa et al. 2015). For the VCA-NLFFF code, we varied the FOV from FOV = $0.08 R_{\odot}$ (which is focused on the strong-field region) to FOV = $0.14 R_{\odot}$ (which includes a larger portion of weak-field regions in the quiet Sun), but found no significant change in the misalignment angle, i.e., $\mu_2(FOV = 0.08) =$ 7.6 ± 6.8 versus μ_2 (FOV = 0.14) = 8.4 ± 7.4 , with a very similar time evolution of the free energy in both cases (Figure 23(n)). Since the VCA-NLFFF code is designed to reject "false" (including noisy) loop tracings with large misalignments $\mu_2 \gtrsim 20^{\circ}$ (Section 5.2), weak-field regions do not introduce larger uncertainties in the VCA-NLFFF solutions, in contrast to W-NLFFF solutions.

6.3. Open Problems: Questions and Answers

Although this benchmark test of the VCA-NLFFF code presented here is the most comprehensive performance test carried out to date, which demonstrates encouraging results, there are still a number of open problems that should be pursued in future studies. These open problems concern fundamental limitations of the VCA-NLFFF method, such as:

- (1) the suitability of the magnetic model; (2) the fidelity of automated feature tracking; (3) the sensitivity to non-potential-field components; (4) the ambiguity of non-potential-field solutions; and (5) the usefulness in practical applications, in particular for forecasting the magnetic evolution of active regions and flares. We discuss these five open issues briefly.
- (1) The magnetic field model used in the VCA-NLFFF model is based on buried magnetic charges and helically twisted field lines (or flux tubes) with an azimuthal field component B_{φ} that is caused by vertical currents at the photospheric boundaries where the unipolar magnetic charges are buried. There are alternative nonlinear force-free magnetic field models, such as that of a sheared arcade (e.g., see the textbooks Priest 1982; Sturrock 1994; Aschwanden 2004), for which an analytical approximation could be derived and fitted to observed loop geometries. In principle, the suitability of such alternative models could be tested by building forward-fitting codes that are equivalent to the VCA-NLFFF code, and by comparing the best-fit misalignment angles between the models and data. More generally, a force-free minimization code such as the W-NLFFF code could be designed that fits coronal loops without using the transverse components at the photospheric boundary. Such a concept was pioneered by Malanushenko et al. (2009, 2011, 2012, 2014), but the major drawbacks of that code using a quasi-Grad-Rubin method is the lack of an automated loop-tracing capability and the prohibitively long computation times.
- (2) The fidelity of automated feature tracking depends on the complexity and noise level of the used EUV and UV images, and whether there are a sufficient number of curvi-linear features that can be detected in the data. The usage of AIA images has demonstrated that the biggest challenge is the elimination of "false" loop tracings, which occur due to insufficient spatial resolution, over-crossing structures, moss structures (Berger et al. 1999; De Pontieu et al. 1999), data noise, and instrumental effects (image edges, vignetting, pixel bleeding, saturation, entrance filter mask, etc.). The usage of IRIS and IBIS images, which have 4-6 times higher spatial resolution than AIA, provide a much larger number of resolved curvi-linear features that are helpful in the reconstruction of the magnetic field, even when they display chromospheric features (fibrils) rather than coronal structures (active region loops and post-flare loops; M. J. Aschwanden et al. 2016, in preparation). Future versions of the VCA-NLFFF code may combine the most suitable features in coronal and chromospheric wavelengths. The free energy is computed in a grid with $\Delta s = 0.002 R_{\odot} \approx 1400$ km resolution, so the grid point with the lowest altitude is located in the photosphere. However, since the line-of-sight field component B_z constrains only the potential field, and the transverse field components B_x , B_y are not used in the VCA-NLFFF code (unlike the W-NLFFF code), the non-force-free conditions of the photosphere do not affect the solution of the VCA-NLFFF code by design, because the field is extrapolated from coronal structures downward to the photosphere.
- (3) The sensitivity to non-potential-field components depends on the availability of detectable curvi-linear features in the penumbral regions of sunspots, where the largest magnetic field strengths occur outside the umbra, while the umbra is generally void of loops and fibrils. The detectability of penumbral structures works best for heliographic locations near the Sun center, while regions far away from the Sun center

generally cause confusion between loops in the foreground and moss structures in the background plages. The accuracy of the total free energy of an active region or flare is dominated by the magnetic field structures near the leading or dominant sunspot, because of the highly nonlinear B^2 -dependence of the free energy on the twisted field. Thus the sensitivity of the VCA-NLFFF code to the free energy is determined by the detectability of structures near the dominant sunspot, in contrast to W-NLFFF codes, where the sensitivity of the free energy is limited by the noise and uncertainty of the transverse field components B_x and B_z in the dominant sunspot region.

- (4) The VCA-NLFFF code has typically $n_{\text{mag}} = 20-100$ magnetic source components, and thus the numerical convergence of the VCA-NLFFF code toward a best-fit solution is in principle not unique, given the uncertainties of automatically traced curvi-linear features. However, we have demonstrated in the parametric study (Section 5.6) that our results are extremely robust when the various control parameters of the VCA-NLFFF code are varied, which implies a stable convergence to the same solution. What we can say about the convergence ambiguity is that the solution is dominated by the strongest magnetic sources, which implies near-unambiguity for the strongest sources (such as the dominant sunspot), while the degree of ambiguity increases progressively for weaker magnetic sources. Since we are mostly interested in the total (volume-integrated) free energy, which is also dominated by the strongest sources due to the B^2 -dependence, the value of the free energy $E_{\text{free}}(t)$ is nearly unambiguous, at any instant of time. As a caveat, the connectivity between positive and negative magnetic polarities should be reliable for strong-field regions, but will break down below a threshold where conjugate magnetic polarities are missing due to the finite number of modeled magnetic sources (in the VCA-NLFFF code) or due to the finite spatial resolution of the magnetogram (in the W-NLFFF code).
- (5) What is the usefulness of the VCA-NLFFF code for practical applications? The main product of the VCA-NLFFF code is the free energy and its time evolution, $E_{\text{free}}(t)$, which includes also estimates of the dissipated magnetic energy during flares, i.e., $E_{\text{diss}} = E_{\text{free}}(t_{\text{end}}) - E_{\text{free}}(t_{\text{start}})$. In principle, other W-NLFFF codes can provide the same information, but their uncertainty is not known, because the inferred values may be affected by the violation of the force-freeness in the photosphere and lower chromosphere, the mismatch between the NLFFF model magnetic field and the observed loops, and the smoothing of the preprocessing technique. Ideally, if the evolution of the free energy can be obtained with either method, this parameter is one of the most relevant quantities for flare forecasting. A machine-learning algorithm called support vector machine has been applied to an HMI data base of 2071 active regions and it was found that the total photospheric magnetic free energy density is the third-best predictor for flares (out of 25 tested quantities), besides the total unsigned current helicity and the total magnitude of the Lorentz force (Bobra & Couvidat 2015).

7. CONCLUSIONS

In this study we present an updated description and performance tests of the VCA-NLFFF code, which is designed to calculate the free energy $E_{\rm free}(t)$ and its time evolution in active regions and flares, after it has been continuously developed over the last five years. This code provides a

complementary and alternative method to existing traditional NLFFF codes, such as the W-NLFFF code (Wiegelmann 2004). The VCA-NLFFF method requires the input of a line-of-sight magnetogram and automated curvi-linear tracing of EUV or UV images in an arbitrary number of wavelengths and instruments. In contrast, the W-NLFFF code requires the input of 3D magnetic field vectors in the photospheric boundary, but has no capability to match observed features in the corona or chromosphere. The performance tests presented here include comparisons of the potential, non-potential, free energy, and flare-dissipated magnetic energy between the VCA-NLFFF and the W-NLFFF code. We summarize the major conclusions.

- The chief advantages of the VCA-NLFFF code over the W-NLFFF code are the circumvention of the unrealistic assumption of a force-free photosphere in the magnetic field extrapolation method, the capability to minimize the misalignment angles between observed coronal loops (or chromospheric fibril structures) and theoretical model field lines, as well as computational speed.
- 2. Comparing 600 W-NLFFF solutions from active region NOAA 11158 and 119 W-NLFFF solutions from 11 X-class flares with VCA-NLFFF solutions we find agreement in the potential, non-potential, and free energy within a factor of ≈1.2, which compares favorably with respect to the range of free energies that have been obtained with other NLFFF codes, scattering by about an order of magnitude for published values of the X2.2 flare in NOAA 11158.
- 3. The time evolution of the free energy $E_{\rm free}(t)$ in 11 X-class flares modeled with both NLFFF codes yields a significant decrease of the free energy during the flare time interval in 10 out of the 11 cases, but the energy amount determined with the W-NLFFF code is statistically a factor of 2 lower, probably because of oversmoothing in the preprocessing technique. In addition we tested the VCA-NLFFF code for 36 C, M, and X-class flares in AR 11158 and detected a significant energy decrease in most cases.
- 4. The amount of magnetic energy decrease during flares agrees within a factor of ≈2-3 between the two NLFFF codes. We suspect that the VCA-NLFFF code fails to detect the full amount of magnetic energy decreases in cases with insufficient loop coverage in penumbral regions. In contrast, the W-NLFFF code may fail to detect the full amount of magnetic energy decreases as a consequence of over-smoothing in the preprocessing procedure and the violation of the force-free condition in the photosphere.
- 5. Both the VCA-NLFFF and the W-NLFFF codes are able to measure the magnetic energy evolution in active regions and the magnetic energy dissipation in flares, but each code has different systematic errors, and thus the two types of codes are truly complementary. The present absolute error in the determination of changes in the free energy during large flares, due to systematic errors, is about a factor of 2, based on the discrepancy between the compared two codes.

The obtained results are encouraging to justify further developments of the VCA-NLFFF code. Future studies may focus on a deeper understanding of the systematic errors of various NLFFF codes, which will narrow down the accuracy of

free energies and flare-dissipated energies. The depth of the buried magnetic charges inferred from the VCA-NLFFF code may give us deeper insights into the solar dynamo and local helioseismology results, an aspect that we have not touched on here. Correlation studies of time series of the free energy may reveal new methods to improve flare forecasting in real time.

7.1. Public Access to VCA-NLFFF Code

The VCA-NLFFF code is also publicly available in the SSW library encoded in the IDL, see website http://www.lmsal.com/~aschwand/software/.

The author is indebted to helpful discussions with Bart De Pontieu, Mark DeRosa, Anna Malanushenko, Carolus Schrijver, Alberto Sainz-Dalda, Ada Ortiz, Jorrit Leenarts, Kevin Reardon, and Dave Jess. Part of the work was supported by the NASA contracts NNG04EA00C of the *SDO*/AIA instrument and NNG09FA40C of the *IRIS* mission.

REFERENCES

```
Alvarado-Gomez, J. D., Buitrago-Cases, J. C., Martinez-Oliveros, J. C., et al.
   2012, SoPh, 280, 335
Amari, T., Boulmezaoud, T. Z., & Aly, J. J. 2006, A&A, 446, 691
Aschwanden, M. J. 2004, Physics of the Solar Corona—An Introduction (New
   York: Praxis and Springer)
Aschwanden, M. J. 2010, SoPh, 262, 399
Aschwanden, M. J. 2013a, SoPh, 287, 323
Aschwanden, M. J. 2013b, SoPh, 287, 369
Aschwanden, M. J. 2013c, ApJ, 763, 115
Aschwanden, M. J. 2015, ApJL, 804, L20
Aschwanden, M. J., Boerner, P., Schrijver, C. J., & Malanushenko, A. 2013a,
  SoPh, 283, 5
Aschwanden, M. J., De Pontieu, B., & Katrukha, E. A. 2013b, Entrp, 15, 3007
Aschwanden, M. J., Lee, J. K., Gary, G. A., Smith, M., & Inhester, B. 2008,
   SoPh, 248, 359
Aschwanden, M. J., & Malanushenko, A. 2013, SoPh, 287, 345
Aschwanden, M. J., & Sandman, A. W. 2010, AJ, 140, 723
Aschwanden, M. J., Sun, X. D., & Liu, Y. 2014a, ApJ, 785, 34
Aschwanden, M. J., Wuelser, J. P., Nitta, N. V., et al. 2012, ApJ, 756, 124
Aschwanden, M. J., Xu, Y., & Jing, J. 2014b, ApJ, 797, 50
Beauregard, L., Verma, M., & Denker, C. 2012, AN, 333, 125
Berger, T. E., De Pontieu, B., Fletcher, L., et al. 1999, SoPh, 190, 409
Bobra, M. G., & Couvidat, S. 2015, ApJ, 798, 135
Cavallini, F. 2006, SoPh, 236, 415
Chintzoglou, G., & Zhang, J. 2013, ApJL, 764, L3
Dalmasse, K., Pariat, E., Valori, G., Demoulin, P., & Green, L. M. 2013, A&A,
   555, L6
De Pontieu, B., Berger, T. E., Schrijver, C. J., & Title, A. M. 1999, SoPh,
De Pontieu, B., Title, A. M., Lemen, J. R., et al. 2014, SoPh, 289, 2733
DeRosa, M. L., Schrijver, C. J., Barnes, G., et al. 2009, ApJ, 696, 1780
DeRosa, M. L., Wheatland, M. S., Leka, K. D., et al. 2015, ApJ, 811, 107
Gary, G. A. 2001, SoPh, 203, 71
Gary, G. A., Hu, Q., Lee, J. K., & Aschwanden, M. J. 2014, SoPh, 289, 3703
Gonzalez, R. C., & Woods, R. F. 2008, Digital Image Processing (Upper
   Saddle River, NJ: Pearson/Prentice-Hall)
Gosain, S. 2012, ApJ, 749, 85
Guerra, J. A., Pulkkinen, A., Uritsky, V. M., & Yashiro, S. 2015, SoPh,
   290, 335
Hoeksema, J. T., Liu, Y., Hayashi, K., et al. 2014, SoPh, 289, 3483
Inoue, S., Hayashi, K., Magara, T., Choe, G. S., & Park, Y. D. 2014, ApJ,
   788, 182
Inoue, S., Hayashi, K., Magara, T., Choe, G. S., & Park, Y. D. 2015, ApJ,
  803, 73
Inoue, S., Hayashi, K., Shiota, D., Magara, T., & Choe, G. S. 2013, ApJ,
Jain, K., Tripathy, S. C., & Hill, F. 2015, ApJ, 808, 60
```

```
Jess, D. B., Mathioudakis, M., Christian, D. J., et al. 2010, SoPh, 261, 363
Jiang, C., & Feng, X. 2013, ApJ, 769, 144
Jiang, J., Zheng, R., Yang, J., et al. 2012, ApJ, 744, 50
Jing, J., Park, S. H., Liu, C., et al. 2012, ApJL, 752, L9
Jing, J., Xu, Y., Lee, J. W., et al. 2015, RAA, 15, 1537
Jing, J., Yuan, Y., Reardon, K., et al. 2011, ApJ, 739, 67
Kazachenko, M. D., Fisher, G. H., Welsch, B. T., Liu, Y., & Sun, X. 2015,
   ApJ, 811, 16
Lemen, J. R., Title, A. M., Akin, D. J., et al. 2012, SoPh, 275, 17
Li, A., & Liu, Y. 2015, SoPh, 290, 2199
Liu, C., Deng, N., Lee, J. W., et al. 2013a, ApJL, 778, L36
Liu, C., Deng, N., Liu, R., et al. 2012, ApJL, 745, L4
Liu, Y., & Schuck, P. W. 2012, ApJ, 761, 105
Liu, Y., Zhao, J., & Schuck, P. W. 2013b, SoPh, 287, 279
Malanushenko, A., Longcope, D. W., & McKenzie, D. E. 2009, ApJ,
   707, 1044
Malanushenko, A., Schrijver, C. J., DeRosa, M. L., & Wheatland, M. S. 2014,
    pJ, 783, 102
Malanushenko, A., Schrijver, C. J., DeRosa, M. L., Wheatland, M. S., &
   Gilchrist, S. A. 2012, ApJ, 756, 153
Malanushenko, A., Yusuf, M. H., & Longcope, D. W. 2011, ApJ, 736, 97
Maurya, R. A., Vemareddy, P., & Ambastha, A. 2012, ApJ, 747, 134
Metcalf, T. R., DeRosa, M. L., Schrijver, C. J., et al. 2008, SoPh, 247, 269
Pesnell, W. D., Thompson, B. J., & Chamberlin, P. C. 2011, SoPh, 275, 3
Petrie, G. J. D. 2012, SoPh, 287, 415
Petrie, G. J. D. 2013, ApJ, 759, 50
Press, W. H., Flannery, B. P., Teukolsky, S. A., & Vetterling, W. T. 1986,
   Numerical Recipes. The Art of Scientific Computing (Cambridge:
   Cambridge Univ. Press)
Priest, E. R. 1982, Solar Magnetohydrodynamics (Dordrecht: Reidel)
Raja, B. A., Kumar, B., Venkatakrishnan, P., et al. 2014, RAA, 14, 207
Sandman, A. W., & Aschwanden, M. J. 2011, SoPh, 270, 503
Sandman, A. W., Aschwanden, M. J., DeRosa, M. L., Wuelser, J. P., &
   Alexander, D. 2009, SoPh, 259, 1
Scherrer, P. H., Schou, J., Bush, R. I., et al. 2012, SoPh, 275, 207
Schrijver, C. J., Aulanier, G., Title, A. M., Pariat, E., & Delanee, C. 2011, ApJ,
  738, 167
Shen, J., Ji, H., Wiegelmann, T., & Inhester, B. 2013, ApJ, 764, 86
Song, Q., Zhang, J., Yang, S. H., & Liu, Y. 2013, RAA, 13, 226
Sorriso-Valvo, L., De Vita, G., Kazachenko, M. D., et al. 2015, ApJ, 801, 36
Sturrock, P. A. 1994, Plasma Physics. An Introduction to the Theory of
   Astrophysical, Geophysical, and Laboratory Plasmas (Cambridge:
   Cambridge Univ. Press)
Sun, X., Bobra, M. G., Hoeksema, J. T., et al. 2015, ApJL, 804, L28
Sun, X., Hoeksema, J. T., Liu, Y., et al. 2012a, ApJ, 748, 77
Sun, X., Hoeksema, J. T., Liu, Y., Chen, Q., & Hayashi, K. 2012b, ApJ,
   757, 149
Tarr, L., Longcope, D., & Millhouse, M. 2013, ApJ, 770, 4
Thompson, W. T. 2006, A&A, 449, 791
Toriumi, S., Iida, Y., Bamba, Y., et al. 2013, ApJ, 773, 128
Toriumi, S., Iida, Y., Kusano, K., & Imada, S. 2014, SoPh, 289, 3351
Tziotziou, K., Georgoulis, M. K., & Liu, Y. 2013, ApJ, 772, 115
Valori, G., Kliem, B., & Fuhrmann, M. 2007, SoPh, 245, 263
Valori, G., Kliem, B., Toeroek., T., & Titov, S. 2010, A&A, 519, A44
Vemareddy, P., Ambastha, A., & Maurya, R. A. 2012a, ApJ, 761, 60
Vemareddy, P., Ambastha, A., Maurya, R. A., & Chae, J. 2012b, ApJ,
Vemareddy, P., Ambastha, A., & Wiegelmann, T. 2013, BASI, 41, 183
Vemareddy, P., Venkatakrishnan, P., & Karthikreddy, S. 2015, RAA, 15, 1547
Wang, R., Yan, Y., & Tan, B. 2013, SoPh, 288, 507
Wang, S., Liu, C., Deng, N., & Wang, H. 2014, ApJL, 782, L31
Wang, S., Liu, C., Liu, R., et al. 2012, ApJL, 745, L17
Wheatland, M. S. 2007, SoPh, 245, 251
Wheatland, M. S., Sturrock, P. A., & Roumeliotis, G. 2000, ApJ, 540, 1150
Wiegelmann, T. 2004, SoPh, 219, 87
Wiegelmann, T., & Inhester, B. 2010, A&A, 516, A107
Wiegelmann, T., Inhester, B., & Sakurai, T. 2006, SoPh, 233, 215
Wiegelmann, T., Thalmann, J. K., Schrijver, C. J., DeRosa, M. L., &
   Metcalf, T. R. 2008, SoPh, 247, 249
Young, P. R., Doschek, G. A., Warren, H. P., & Hara, H. 2013, ApJ, 766
Zhang, H., Brandenburg, A., & Sokoloff, D. D. 2014, ApJL, 784, L45
Zhao, J., Li, H., Pariat, E., et al. 2014, ApJ, 787, 88
```